New Phytologist

Research

Molecular and electrophysiological characterization of anion transport in *Arabidopsis thaliana* pollen reveals regulatory roles for pH, Ca^{2+} and GABA

Patrícia Domingos[1,2]*, Pedro N. Dias[1,2]*, Bárbara Tavares[2], Maria Teresa Portes[1,2], Michael M. Wudick[1], Kai R. Konrad[3], Matthew Gilliham[4], Ana Bicho[2†] and José A. Feijó[1,2]

[1]Department of Cell Biology and Molecular Genetics, University of Maryland, 0118 Bioscience Research Building, 4066 Campus Dr. College Park, College Park, MD 20742-5815, USA; [2]Instituto Gulbenkian de Ciência, Oeiras 2780-901, Portugal; [3]Department of Botany I, Julius-Von-Sachs Institute for Biosciences, University of Würzburg, Würzburg 97082, Germany; [4]Australian Research Council Centre of Excellence in Plant Energy Biology, Waite Research Institute & School of Agriculture, Food and Wine, University of Adelaide, Glen Osmond, SA 5064, Australia

Author for correspondence:
José A. Feijó
Tel: +1 301 405 9746
Email: jfeijo@umd.edu

Received: *27 January 2019*
Accepted: *11 April 2019*

New Phytologist (2019)
doi: 10.1111/nph.15863

Key words: anion transport, Arabidopsis, AtALTMT12, AtCCC, AtSLAH3, AtTMEM16, electrophysiology, pollen.

Summary

- We investigated the molecular basis and physiological implications of anion transport during pollen tube (PT) growth in *Arabidopsis thaliana* (Col-0).
- Patch-clamp whole-cell configuration analysis of pollen grain protoplasts revealed three subpopulations of anionic currents differentially regulated by cytoplasmic calcium ($[Ca^{2+}]_{cyt}$). We investigated the pollen-expressed proteins *At*SLAH3, *At*ALMT12, *At*TMEM16 and *At*CCC as the putative anion transporters responsible for these currents.
- *At*CCC-GFP was observed at the shank and *At*SLAH3-GFP at the tip and shank of the PT plasma membrane. Both are likely to carry the majority of anion current at negative potentials, as extracellular anionic fluxes measured at the tip of PTs with an anion vibrating probe were significantly lower in *slah3*$^{-/-}$ and *ccc*$^{-/-}$ mutants, but unaffected in *almt12*$^{-/-}$ and *tmem16*$^{-/-}$. We further characterised the effect of pH and GABA by patch clamp. Strong regulation by extracellular pH was observed in the wild-type, but not in *tmem16*$^{-/-}$. Our results are compatible with *At*TMEM16 functioning as an anion/H^+ cotransporter and therefore, as a putative pH sensor. GABA presence: (1) inhibited the overall currents, an effect that is abrogated in the *almt12*$^{-/-}$ and (2) reduced the current in *At*ALMT12 transfected COS-7 cells, strongly suggesting the direct interaction of GABA with *At*ALMT12.
- Our data show that *At*SLAH3 and *At*CCC activity is sufficient to explain the major component of extracellular anion fluxes, and unveils a possible regulatory system linking PT growth modulation by pH, GABA, and $[Ca^{2+}]_{cyt}$ through anionic transporters.

Introduction

Pollen tubes (PTs) are dramatically polarised cells that grow exclusively in the apex and respond to specific female cues to grow towards the ovule (Boavida *et al.*, 2005; Feijó, 2010). Previously, we characterised chloride (Cl^-) fluxes in growing PTs of lily (*Lilium longiflorum*) and tobacco (*Nicotiana tabacum*) by extracellular anion-specific vibrating probes and showed that, in both species, PTs display massive oscillatory Cl^- effluxes at the tip and stable influxes along the shank (Zonia *et al.*, 2002). These fluxes are essential to PT growth and we hypothesised these to contribute to osmoregulation by carrying water on the anion's hydration shells. Subsequently, using patch clamp, we described three distinct anion currents regulated by cytoplasmic calcium ($[Ca^{2+}]_{cyt}$ on lily pollen protoplasts) (Tavares *et al.*, 2011a). These currents were quantitatively and qualitatively consistent with the anion fluxes previously reported (Zonia *et al.*, 2002), but the molecular nature of their underlying channels remains unaccounted for.

The mechanosensitive channel *At*MSL8 stands to date as the only anion channel implicated in pollen grain (PG) rehydration and germination of Arabidopsis (Hamilton *et al.*, 2015). Other candidates for anion currents in PTs have been postulated from pollen transcriptomics (Pina *et al.*, 2005; Boavida *et al.*, 2011; Tavares *et al.*, 2011b). *AtSLAH3* (*SLow Anion channel-associated 1 Homolog 3*) is highly expressed in the PGs and PTs, and was

*These authors contributed equally to this work.
†This paper is dedicated to the memory of Ana Bicho, who started the project and was responsible for the early supervision of PD, PND and BT.

the first anion channel gene to be shown to regulate PT growth via modulation of various calcium-dependent protein kinases (CPKs) (Gutermuth *et al.*, 2013, 2018). Other PT candidates include *ALMT12* (Aluminum-Activated Malate Transporter 12) and *At1g73020* (Pina *et al.*, 2005; Gutermuth *et al.*, 2013, 2018). The last one shows sequence homology with Trans Membrane Protein 16 (TMEM16) or anoctamin (ANO) protein family, previously identified as Ca^{2+}-activated Cl^- channels (CaCC) in mammalians (ANO1 and ANO2) (Caputo *et al.*, 2008; Schroeder *et al.*, 2008; Yang *et al.*, 2008). Their roles and structure have been described in detail (Pedemonte & Galietta, 2014; Courjaret *et al.*, 2016; Paulino *et al.*, 2017). *At*SLAH3 and *At*ALMT12 channels in guard cells, and TMEM16/CaCC in mammalian cells, present strong voltage dependence, are activated by a wide range of membrane potentials (V_m), and the amplitude of their current is dependent on extracellular Cl^- concentration ($[Cl^-]_{out}$) (Caputo *et al.*, 2008; Schroeder *et al.*, 2008; Yang *et al.*, 2008; Meyer *et al.*, 2010; Geiger *et al.*, 2011). These features show a resemblance to the currents found in PG protoplasts from fully hydrated PGs or PTs of lily (Tavares *et al.*, 2011a). The cation-chloride cotransporter *AtCCC* was also found to be highly expressed in pollen and influences Na^+ and Cl^- transport from root to shoots (Colmenero-Flores *et al.*, 2007; Henderson *et al.*, 2015). $ccc^{-/-}$ has a reproductive phenotype (Colmenero-Flores *et al.*, 2007), making it another putative carrier of the anion fluxes across pollen membranes.

Here, we characterised the molecular basis of anion transport in the pollen of *Arabidopsis thaliana* (Col-0). We investigated the roles of *At*SLAH3, *At*ALMT12, *At*TMEM16 and *At*CCC as the putative transporters responsible for the anionic fluxes and currents described in wild-type (WT) fully hydrated pollen protoplasts. Based on phenotypes and extracellular fluxes of null mutants and transporter localisation, we concluded that *At*SLAH3 and *At*CCC activity is likely to account for the majority of the anion fluxes observed across PTs. Furthermore, we investigated the possible regulatory role of pH, Ca^{2+}, and GABA on the anionic currents present in pollen protoplasts. We observed that GABA inhibits anionic currents and we present the first genetic evidence that *At*ALMT12 is a GABA receptor. Furthermore, we provide the first characterisation of *At*TMEM16 in plants, and demonstrated that it acts as an H^+/anion cotransporter in pollen.

Materials and Methods

Plants, culture conditions and pollen grain collection

Arabidopsis thaliana (L.) Heynh. Wild-type seeds (WT), ecotype Columbia (Col-0), were obtained from the Nottingham Arabidopsis Stock Centre (NASC). The mutant lines used in this study were obtained from NASC or kindly provided. All plants were grown for seed as described in Prado *et al.* (2008). Seeds from mutant lines were germinated in Murashige and Skoog (MS) medium complemented with kanamycin (50 μg ml^{-1}) or sulfadiazine (Gabi-kat, 7.5 mg ml^{-1}). The insecticide Destroyer 5G (5% w/w chlorpyrifos; Agriphar, Ougree, Belgique) was used. Detailed information is available in Supporting Information Methods S1.

Identification of *A. thaliana* mutant lines and generation of transgenics

Genomic DNA was extracted according to Edwards *et al.* (1991) and Cenis (1992). All chemicals and molecular biology material were purchased from Sigma Aldrich and New England BioLabs (Ipswich, MA, USA), unless otherwise stated. Detailed information of the selected genes and the mutant lines morphological analysis is available in Methods S2. Table S1 depicts the primer pairs constructed to identify the mutant plants and amplify the full genomic sequence of the candidate transporters. Gateway Cloning System (Thermo Scientific, Waltham, MA, USA) was used according to manufacturer instructions. Arabidopsis (Col-0) plants were transformed via the *Agrobacterium tumefaciens*-mediated floral dip method (Clough & Bent, 1998). Transgenic plants were selected by scoring the presence of GFP-positive pollen.

Cell line culture and transient transfection

The coding sequence for *At*ALMT12 was cloned into the pCI mammalian expression vector under the cytomegalovirus (CMV) promoter. African Green Monkey Kidney cells (COS-7; ATCC, CRL-1651) were acquired from the American Type Culture Collection. Detailed information of cell culture and transfection conditions available in Methods S3.

Live-cell and confocal imaging

Images from *A. thaliana* (Col-0) transgenic PTs were acquired on an Applied Precision Deltavision CORE system (Olympus Europa SE & Co. KG, Olympus Life Sciences, Hamburg, Germany), mounted on an Olympus inverted microscope, equipped with a Cascade II 2014 EM-CCD camera (Teledyne Photometrics, Tucson, AZ, USA), using the ×100 Uplan SAPO 1.4NA oil immersion objective (Olympus Europa) or the ×60 1.2NA water immersion objective, green and red filter sets and differential interference contrast (DIC) optics (detailed in Methods S4).

Protoplast isolation

The experimental protocol was adapted from Tanaka *et al.* (1987), Fan *et al.* (2001), Mouline *et al.* (2002) and Tavares *et al.* (2011a) (full description in Methods S5).

Electrophysiology

Currents from pollen protoplasts were measured and normalised as described in Tavares *et al.* (2011a). Seal resistance was > 2 GΩ. The voltage protocols used to study current activation and current deactivation (I_{tail}) are shown as insets in Fig. 1(a) and Fig. 1 (h), respectively. In both protocols, the cell membrane was kept at a holding potential of −100 mV. The micropipettes and the reference electrode were produced as described in Tavares *et al.*(2011a). The composition of intracellular and extracellular solutions is shown in Table S2. The inhibitory effect of 5-nitro-2-(3-phenylpropylamino)benzoic acid (NPPB), a known

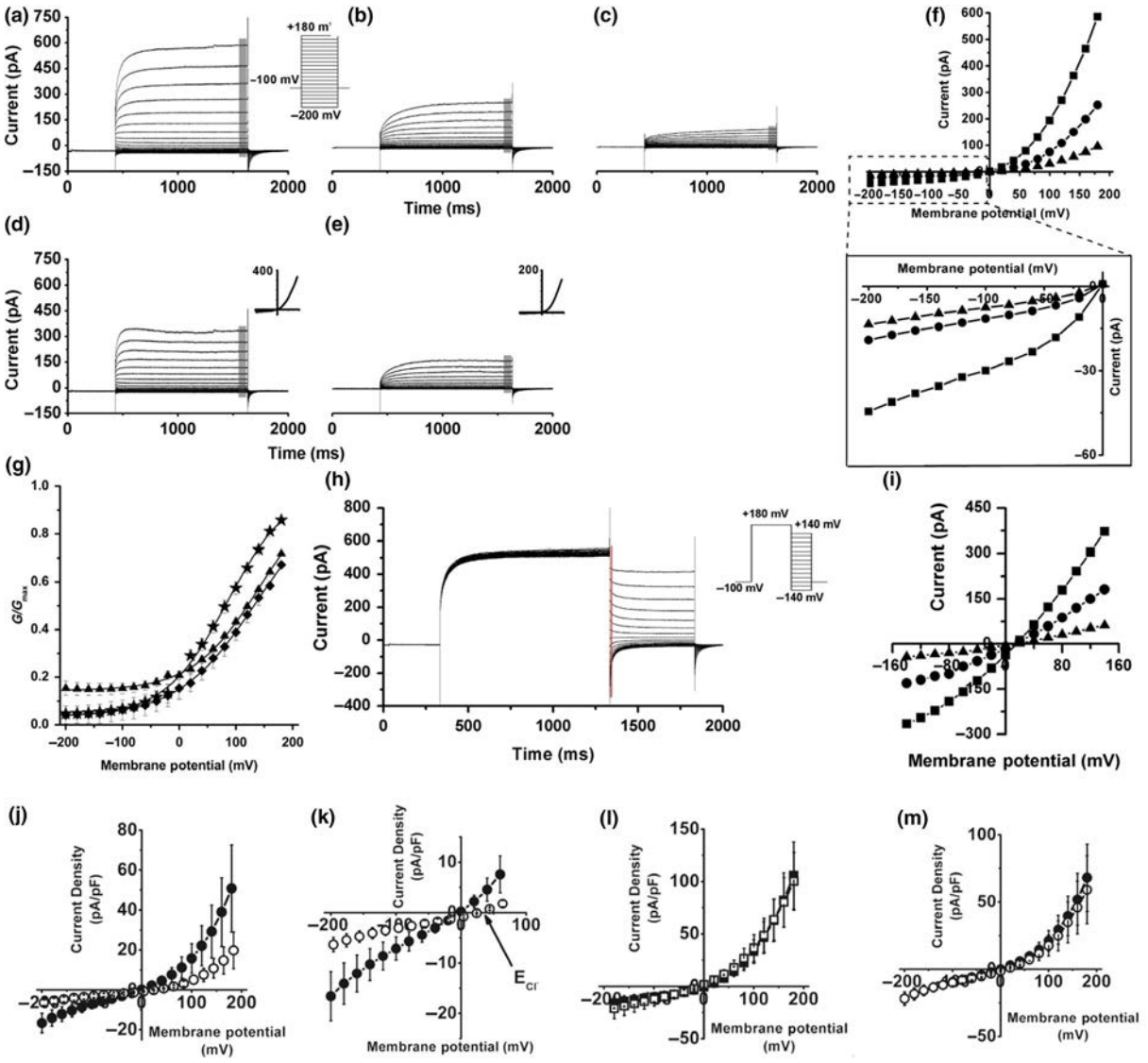

Fig. 1 Typical anionic whole-cell (WC) currents from pollen grain protoplasts of *Arabidopsis thaliana*, measured with Bath/Pipette B1/P1 solutions (control group, *n*M $[Ca^{2+}]_{cyt}$). The currents were elicited from a holding potential of −100 mV with the activation voltage protocol represented as an inset in (a). (a–e) Raw data obtained from one protoplast. (a) Initial current recorded immediately after entering whole-cell configuration ($I_{initial}$). (b) Current recorded after rundown (I_{final}), 72 min after entering whole-cell configuration. (c) Current recorded after inhibition by 100 μM of 5-nitro-2-(3-phenylpropylamino) benzoic acid (NPPB) (I_{NPPB}). (d) Current lost during rundown ($I_{rundown}$) obtained by subtracting $I_{initial}$ and I_{final}. (e) Inhibited current ($I_{inhibited}$) obtained by subtracting I_{final} and I_{NPPB}. (f) Current–voltage (*I*/*V*) relationships of $I_{initial}$ (squares), I_{final} (circles), and I_{NPPB} (triangles) constructed with the steady-state current (I_{ss}), values were averaged from the last 50 ms of the respective raw data (grey line). It is possible to observe the decrease in the current amplitude before and after rundown, but also the reduction caused by the inhibitor NPPB. Both reductions occurred for negative and positive V_m. The inserts in (d) and (e) represent their respective *I*/*V* curves constructed with the I_{ss} values, averaged from the last 50 ms of the raw data (grey lines). (g) Voltage dependence of the averaged normalised chord conductance (G/G_{max}) obtained for $I_{rundown}$ (star), I_{NPPB} (triangle), and $I_{inhibited}$ (rhombus). These values were calculated using Eqn 2. (h) Typical raw data for the WC deactivation current ($I_{initial}$). Currents were measured with a deactivation voltage protocol (inset). (i) *I*/*V* curve of $I_{initial}$ (squares), I_{final} (circles), and I_{NPPB} (triangles), constructed from the current values obtained immediately after the test potential was applied (I_{tail}; red line). (j) Average normalised *I*/*V* curves obtained during Bath Solution Exchange 1 experiment either before (circles, B1; $[Cl^-] = 140$ mM + $[NO_3^-] = 5$ mM) or after the substitution of the external solution (open circles, B2; $[Cl^-] = 27$ mM + $[NO_3^-] = 5$ mM; $n = 5$). It is possible to observe the reduction in current intensity for the positive and negative currents. (k) Detail of the negative currents from *I*/*V* curve in (j). The arrow shows the expected equilibrium potential for chloride (E_{Cl-}) for the B2/P1 combination. (l) Average normalised *I*/*V* curves obtained for Bath Solution Exchange 2 either before (squares; B1, $[Cl^-] = 140$ mM + $[NO_3^-] = 5$ mM) or after the substitution of the external solution (open squares; B3, $[Cl^-] = 31$ mM + $[NO_3^-] = 110$ mM; $n = 6$). (m) Average normalised *I*/*V* curves obtained before (circles; B4, $[NO_3^-] = 140$ mM + $[Cl^-] = 5$ mM) and after the substitution of the external solution (open circles; B5, $[NO_3^-] = 31$ mM + $[Cl^-] = 110$ mM; $n = 6$). All currents were elicited from a holding potential of −100 mV with the activation voltage protocol. The *I*/*V* traces were built with the steady-state currents (I_{ss}), averaged from the last 50 ms of the raw data, normalised with the capacitance of each cell. (m–j) Data are represented as mean ± SE. *, $P < 0.05$;

inhibitor of anionic currents (Gögelein, 1988), was tested on the currents. The effect of the solvent DMSO and TEA^+ on the anionic currents was studied and found to have no impact.

In the assays performed with mammalian cells, a voltage protocol with a prepulse of +40 mV was chosen to maintain the *At*ALMT12 expressing mammalian cells at their minimum state of conductivity (Meyer *et al.*, 2010). The inhibitory effect of indanyloxyacetic acid (IAA) 94 mammalian Cl^- channel blocker was also tested to confirm the anionic nature of the currents (full description of the voltage protocols used and the anion-selective self-referencing probe analysis of Cl^- fluxes in germinated pollen in Methods S6 and S7, respectively).

Data analysis

Data analysis was performed as described in Tavares *et al.* (2011a). Current–voltage (*I/V*) relationships were produced using the current density values (pA/pF), obtained by normalising the currents with their respective membrane capacitance (C_m). For each experimental condition data from different cells were averaged. The data shown are mean ± SE (n), where n is the number of cells studied. Statistical significances were determined using *t*-test with ORIGIN 6.1 software (OriginLab Corp., Northampton, MA, USA), unless stated otherwise, and differences were considered significant if $P < 0.05$. Equilibrium potentials for the ions in solution were calculated with the Nernst equation (Table S3; more details in Methods S8).

Results

Arabidopsis thaliana pollen protoplasts generate outward-rectifying, depolarisation-activated anionic currents regulated by cytoplasmic [Ca^{2+}]

We used the whole-cell (WC) patch-clamp technique to investigate anionic currents in pollen protoplasts of Arabidopsis (Col-0), under symmetrical anionic concentrations of [Cl^-] = 140 mM and [NO_3^-] = 5 mM. We refer to the control condition as B1/P1, and all media variations follow this pairwise notation, where Bath = B*x* and Pipette = P*x* (Table S2).

When we clamped protoplasts using the voltage protocol shown on inset of Fig. 1(a) an influx of anions (that is outwardly rectifying anionic currents) was systematically elicited for positive potentials. This influx was time-dependent at positive potentials, but a gradual decrease of the initial currents, or rundown, was always observed (representative traces shown in Fig. 1a for the initial current – $I_{initial}$ and Fig. 1b for the current after rundown – I_{final}). This behaviour is generally accepted to be due to dilution of intracellular regulators necessary for sustained activation (Marty & Neher, 1995; Becq, 1996; Binder *et al.*, 2003). The rundown period varied from 30 to 180 min ($I_{rundown}$ – Fig. 1d calculated by point-by-point subtraction of $I_{initial}$ from I_{final}). To simplify analysis, we used the current values obtained at −160 and +160 mV and estimated the percentage of current rundown (%Rundown) as 48 ± 3% and 55 ± 3% respectively (Table 1). Further channel profiling was done after rundown using pharmacology, and we found the anion channel inhibitor NPPB

Table 1 Anion current parameters calculated for wild-type Col-0 *Arabidopsis thaliana* and for the different mutant lines, *tmem16*$^{-/-}$, *almt12*$^{-/-}$, *slah3*$^{-/-}$, and *almt12*$^{-/-}$;*slah3*$^{-/-}$ obtained immediately after entering the whole-cell configuration in Bath/Pipette B1/P1 solutions measured at ± 160 mV.

	WT				*tmem16*$^{-/-}$				*almt12*$^{-/-}$				*slah3*$^{-/-}$				*almt12*$^{-/-}$;*slah3*$^{-/-}$			
	$I_{(-160\ mV)}$	$I_{(+160\ mV)}$	V_{rev}	n	$I_{(-160\ mV)}$	$I_{(+160\ mV)}$	V_{rev}	n	$I_{(-160\ mV)}$	$I_{(+160\ mV)}$	V_{rev}	n	$I_{(-160\ mV)}$	$I_{(+160\ mV)}$	V_{rev}	n	$I_{(-160\ mV)}$	$I_{(+160\ mV)}$	V_{rev}	n
$I_{initial}$	−78 ± 11	365 ± 51	−2.1 ± 0.7	53	−145 ± 37¥	542 ± 69	−0.6 ± 1.3	24	−81 ± 15¥	421 ± 29	−0.3 ± 0.3	5	−135 ± 26¥	907 ± 127¥	−10 ± 5.6¥	13	−49 ± 10¥	460 ± 33	−9.5 ± 2.5¥	5
I_{final}	−41 ± 7	162 ± 45	−2.0 ± 1.2	53	−62.5 ± 33¥	226 ± 71¥	0.2 ± 2.8	24	−28 ± 4¥	210 ± 37	−5.5 ± 0.9	4	−48 ± 9	350 ± 95¥	3.2 ± 2.3¥	13	−11 ± 2.6¥	211 ± 26	−6 ± 7	5
$I_{rundown}$	−36 ± 11	207 ± 32	18 ± 1*	53	−61 ± 25¥	404 ± 61¥	4.4 ± 3.8¥	24	−51 ± 20	235 ± 45	3.7 ± 1.4¥	4	−80 ± 22¥	532 ± 88¥	−4.5 ± 2.3¥	12	−38 ± 9.6¥	248.9 ± 53	−12 ± 2¥	5
$I_{inhibited}$	−26 ± 21	53 ± 10	−8 ± 13	5	−1.7 ± 0.0¥	13 ± 10¥	3 ± 7	3	−4 ± 2¥	42 ± 12	−4.3 ± 1.4	3	−2.6 ± 3.2¥	37 ± 19	9.7 ± 7.5¥	4	−1 ± 0.4¥	11.9 ± 2.9¥	−20 ± 14	5
% RD	48 ± 3	55 ± 3		53	56 ± 5	58 ± 5		20	63 ± 9¥	52 ± 9		4	62 ± 7¥	62 ± 6¥		12	76.5 ± 6.0¥	52 ± 8		5
% Inhib.	48 ± 21	38 ± 8		5	–	4.7 ± 2.5¥		3	14 ± 7¥	18 ± 4¥		3	–	6 ± 3¥		4	10 ± 1.2¥	6.4 ± 2.1¥		5
	g_{in}	g_{out}	$g_{in}:g_{out}$	n	g_{in}	g_{out}	$g_{in}:g_{out}$	n	g_{in}	g_{out}	$g_{in}:g_{out}$	n	g_{in}	g_{out}	$g_{in}:g_{out}$	n	g_{in}	g_{out}	$g_{in}:g_{out}$	n
$I_{initial}$	41.4 ± 4.6	5.4 ± 1.2	19.8 ± 2.0	53	54.9 ± 7.6¥	8.7 ± 2.5	16.2 ± 2.7	24	31.7 ± 0.5*¥	4.0 ± 0.08	12.0 ± 3.4	5	70 ± 0.9¥	6 ± 0.1	23 ± 9	13	48 ± 0.2	2 ± 0.04¥	25.4 ± 4.2	5
I_{final}	30 ± 4.7*	3.6 ± 0.8	14.8 ± 1.8*	53	28.4 ± 5.5*	4.4 ± 1.4	25.7 ± 7.6*¥	24	22 ± 0.3¥	0.08 ± 0.02¥	31 ± 7¥	4	36 ± 0.6	3 ± 0.08	17.5 ± 3.0	12	28 ± 0.4	0.4 ± 0.01¥	81 ± 19¥	5
$I_{rundown}$	20 ± 0.4	3 ± 0.07	12 ± 3*	27	30 ± 0.6	4 ± 0.2	10 ± 3*	20	16 ± 0.7	2.4 ± 0.08	10 ± 5	4	45 ± 0.7	4 ± 0.1	17 ± 4.6	12	20 ± 0.6	2 ± 0.04	14 ± 3.4	5
$I_{inhibited}$	0.5 ± 0.04*	0.08 ± 0.05*	5.6 ± 8*	5	0.2 ± 0.1	–	–	3	0.3 ± 0.09*	–	–	3	0.4 ± 0.2*	–	–	4	0.13 ± 0.02*	0.004 ± 0.006¥	0.13 ± 6.6*	5

%Inhib., percentage of inhibited current; %RD, percentage of current lost during rundown; $[NPPB]_{max}$, 5-nitro-2-(3-phenylpropylamino)benzoic acid maximum concentration tested (100 μM); g_{in} (nS), inward conductance; $g_{in}:g_{out}$, inward conductance (g_{in}) and the outward conductance (g_{out}) ratio; g_{out} (nS), outward conductance; I_{final}, current density (pA/pF) measured after rundown; $I_{inhibited}$, inhibited current density (pA/pF); $I_{initial}$, initial current density (pA/pF) measured after entering whole-cell configuration; $I_{rundown}$, current density (pA/pF) lost during rundown; V_{rev}, reversal potential (mV); WT, wild-type.
Data are represented as mean ± SE.
*, ¥, Statistically significant differences between comparable parameters within the same table column. ¥, Significant differences between comparable parameters between WT and mutants ($P < 0.05$).

(100 μM) to inhibit currents at both −160 and +160 mV by 48 ± 21 and 38 ± 8%, respectively (Tables 1, S4). This inhibition is plotted in Fig. 1(c), representing the current remaining after NPPB (I_{NPPB}), and Fig. 1(e), representing the current supressed by NPPB ($I_{inhibited}$). This general pattern of behaviour of anion currents in Arabidopsis protoplasts is summarised on the *I*/*V* (current/voltage) curves shown for $I_{initial}$, I_{final} and I_{NPPB} in Fig. 1(f), where the steady-state currents (I_{ss}) were averaged from the last 50 ms of the raw data (Fig. 1a–e, grey vertical bars). Of relevance, the reversal potentials (−2.1 ± 0.7, −2.0 ± 1.2 mV, −5.0 ± 0.8, respectively) were all close to the expected value for E_{Cl^-} and $E_{NO_3^-}$ (0 mV; Table S3), supporting the conclusion that they are essentially generated by anions. Both anion influxes and effluxes (negative or inward-rectifying currents) exhibit rundown and were partially inhibited by NPPB (top and bottom part of Fig. 1f, respectively). The data suggest that the channels underlying these currents have weak rectification properties, supporting both influx and efflux depending on membrane potential (summary of the quantitative parameters in Tables 1, S4). To achieve more detail on the electrophysiological parameters of the observed currents, we calculated the influx/inward conductance (g_{in}) and the efflux/outward conductance (g_{out}). The ratio of $g_{in} : g_{out}$ values were found to be significantly higher in $I_{initial}$ (19.8 ± 2, Table 1), indicative of stronger rectification for depolarising potentials, and allowing outward currents to pass through the channels more easily than inward currents. To further illustrate the behaviour of the channels responsible for the observed currents under different V_m we calculated the normalised chord conductance (G/G_{max} values calculated using Eqn 2 described in Methods S8). Fig. 1(g) shows the results for $I_{rundown}$, I_{NPPB} and $I_{inhibited}$, hinting at distinct sensitivities to variations of V_m values, particularly in $I_{rundown}$ (similar effect observed in lily; Tavares *et al.*, 2011a). Finally, Cl^- and Ca^{2+} have been proposed to be functionally linked through the anion channels *At*SLAH3 (Gutermuth *et al.*, 2013) and *At*ALMT12,13 and 14 (Gutermuth *et al.*, 2018). Therefore, we tested the influence of different internal $[Ca^{2+}]_{cyt}$, designated as μCa (B1/P2) and mCa (B1/P3), using the activation protocol depicted in Fig. 1(a) ($[Ca^{2+}]_{free}$ in Table S2). The variations of the average $I_{rundown}$, I_{NPPB} and $I_{inhibited}$ are depicted in Fig. S1; Tables 1, S4. An extra set of experiments was designed to further confirm the anionic nature of the currents, by lowering the extracellular $[Cl^-]$ ($[Cl^-]_{out}$) from 140 mM $[Cl^-]$ + 5 mM $[NO_3^-]$ to 27 mM $[Cl^-]$ + 5 mM $[NO_3^-]$ (Fig. 1j,k); BSE1 in Tables S2, S5; BSE stands for 'Bath Solution Exchange'. Overall, these results demonstrated that: (1) higher $[Ca^{2+}]_{cyt}$ increases the population of open channels and, (2) NO_3^- and Cl^- are the major contributors to the I_{ss} described (additional analysis of the effect of Ca^{2+} and reduced $[Cl^-]$ in the currents is available in Fig. S1; Tables S4, S5).

The anionic plasma membrane channels are more permeable to NO_3^- than to Cl^-

Most plant anion channels show a preferential permeability for NO_3^- over Cl^-, which we addressed by Bath Solution Exchange experiments (BSE2: B1/P1 → B3 and BSE3: B4/P4 → B5; Table S3), after current stabilisation. These were designed to determine P_{NO_3}/P_{Cl} for I_{final} and $I_{rundown}$ (detailed in Table S5), going from the initial $[Cl^-]_{out}$ ($[Cl^-]$ = 140 mM + $[NO_3^-]$ = 5 mM) to $[NO_3^-]_{out}$ ($[Cl^-]$ = 31 mM + $[NO_3^-]$ = 110 mM). In the reverse experiment (BSE3), NO_3^- was enriched in the external and internal solutions (B4/P4;$[NO_3^-]$ = 140 mM + $[Cl^-]$ = 5 mM), and after rundown $[NO_3^-]_{out}$ was partially replaced by $[Cl^-]_{out}$($[NO_3^-]$ = 31 mM + $[Cl^-]$ = 110 mM. Average *I*/*V* curves obtained before and after the substitution in BSE2 (n = 6) and BSE3 (n = 6) are shown in Fig. 1(lv–m). Currents, conductivity (g_{out} and g_{in}) and rectification ($g_{in} : g_{out}$) did not change significantly (Table S5). P_{NO_3}/P_{Cl} was 2.3 ± 0.9 and 1.7 ± 0.1, in BSE2 and BSE3, indicating that these channels are approximately twice as permeable to NO_3^- than to Cl^-. A significantly stronger rectification in the current elicited before and after the exchange of solution indicates regulation by the permeable ion (Table S5, I_{before} and I_{after} in BSE2 and BSE3). Irrespectively, the general kinetic features and voltage dependency in the presence of NO_3^--based solutions were similar, suggestive that these two anions are permeating the same channels.

Different channel contributions to pollen anionic currents in Arabidopsis

Transcriptomic search in *A. thaliana* PG and PT for channel families with electrophysiological or transport features that would fit the observations in both lily and Arabidopsis led us to select four candidate genes for a reverse genetics approach: *At*CCC, *At*SLAH3, *At*ALMT12 and *At*TMEM16. Loss-of-function pollen protoplasts of all four candidates were characterised by means of electrophysiological techniques.

Null alleles of *ccc*$^{-/-}$ *and tmem16*$^{-/-}$ single mutants, and of the *tmem16*$^{-/-}$; *ccc*$^{-/-}$ double mutant were patch clamped but no significant differences in currents from WT were detected. Likewise, the raw data obtained for *tmem16*$^{-/-}$, *almt12*$^{-/-}$, *slah3*$^{-/-}$, and *slah3*$^{-/-}$;*almt12*$^{-/-}$ mutants depicted a qualitatively WT- similar electrophysiological fingerprint (Tables 1–3), namely time-dependent activation (data not shown), strong outward rectification and rundown. However, closer analysis of the currents derived from I_{ss} obtained in the negative V_m range revealed important differences. Reverse potentials (V_{rev}) measured in WT, *tmem16*$^{-/-}$ and *almt12*$^{-/-}$ for $I_{initial}$ and I_{final} were close to the expected value for E_{Cl^-}, strongly suggesting that these currents were anionic (Cl^- and NO_3^-) (Table 1). By contrast, the V_{rev} measured in *slah3*$^{-/-}$ for $I_{initial}$ presented a significant shift towards a more negative V_m, which was lost in I_{final} (−10.0 ± 5.6 to 3.2 ± 2.3 mV, Table 1). This result suggests that *At*SLAH3 channels may have a role in maintaining the resting potential.

Conversely, the absence of *At*TMEM16 produced a statistically significant increase in $I_{initial}$ for all tested V_m by an average of 86% and 48%, for −160 mV and +160 mV, respectively, mirrored by an increase in %Rundown of 8% and 3% when compared with the WT (Table 1). Similar to *tmem16*$^{-/-}$, *slah3*$^{-/-}$ mutant protoplasts elicited a significant, almost two-fold larger, $I_{initial}$ for the positive V_m and 73% more current for −160 mV,

Table 2 Current parameters for *Arabidopsis thaliana* Col-0 wild-type and *tmem16*$^{-/-}$ mutant under different external pH conditions (pH_{out}), obtained immediately after entering the whole-cell configuration measured at ± 160 mV.

	WT					*tmem16*$^{-/-}$				
	pH_{out} 5.6					pH_{out} 5.6				
	g_{in}	g_{out}	$g_{in}:g_{out}$	V_{rev}	n	g_{in}	g_{out}	$g_{in}:g_{out}$	V_{rev}	n
I_{ss}	52.1 ± 10.9	8.2 ± 3.6*	11.9 ± 4.5	−1.0 ± 1.5	4	28.7 ± 8.2	4.1 ± 2.5	10.9 ± 3.3*	−8.1 ± 3.1	3
I_{inst}	25.9 ± 4.5	12.2 ± 3.0	2.6 ± 0.7	−10.9 ± 3.0*§	4	13.4 ± 4.5	5.6 ± 1.5	2.3 ± 0.3	−29.0 ± 2.8*¥	3
I_{tail}	44.1 ± 11.7	33.1 ± 9.9*	1.4 ± 0.1	9.5 ± 3.4§	3	23.0 ± 5.7	12.6 ± 2.5	2.0 ± 0.8	24.0 ± 22.1	3
	pH_{out} 5.8					pH_{out} 5.8				
	g_{in}	g_{out}	$g_{in}:g_{out}$	V_{rev}	n	g_{in}	g_{out}	$g_{in}:g_{out}$	V_{rev}	n
I_{ss}	30.0 ± 4.7	3.6 ± 0.8	14.8 ± 1.8*	−2.0 ± 1.2*	53	28.4 ± 5.5	4.4 ± 1.4	25.7 ± 7.6*	0.2 ± 2.8*	24
I_{inst}	15.0 ± 2.5*	5.5 ± 1.1	3.8 ± 0.4*	−23.3 ± 1.8*	53	16.9 ± 4.2	6.2 ± 1.6	4.7 ± 1.5*	−25.8 ± 3.5*	24
I_{tail}	23.6 ± 4.2	17.0 ± 3.5*	2.3 ± 0.5*	27.6 ± 5.2*	31	25.9 ± 5.0	17.1 ± 3.1*	1.7 ± 0.3*	35.4 ± 9.2*	20
	pH_{out} 6.0					pH_{out} 6.0				
	g_{in}	g_{out}	$g_{in}:g_{out}$	V_{rev}	n	g_{in}	g_{out}	$g_{in}:g_{out}$	V_{rev}	n
I_{ss}	62.6 ± 12.4*§	8.1 ± 3.7	20.8 ± 4.4*	−1.5 ± 0.9*	8	19.2 ± 9.3¥	2.1 ± 0.7	9.1 ± 2.7*¥	0.2 ± 1.9*	6
I_{inst}	30.0 ± 6.2*§	11.8 ± 4.0	4.3 ± 0.9	−19.2 ± 3.4*	8	6.5 ± 2.6§¥	3.2 ± 1.1	1.8 ± 0.3¥	−32.1 ± 7.1*	6
I_{tail}	30.0 ± 14.8	21.4 ± 13.2	2.6 ± 0.8	13.7 ± 2.2*§	4	14.5 ± 6.2	9.1 ± 4.0	1.8 ± 0.4	44.7 ± 19.1*	6
	pH_{out} 6.4					pH_{out} 6.4				
	g_{in}	g_{out}	$g_{in}:g_{out}$	V_{rev}	n	g_{in}	g_{out}	$g_{in}:g_{out}$	V_{rev}	n
I_{ss}	61.5 ± 14.8§	6.1 ± 2.6	21.4 ± 5.9*	−1.0 ± 0.8	6	18.6 ± 6.4¥	3.1 ± 1.5	8.8 ± 3.0*	−3.1 ± 1.0	6
I_{inst}	29.9 ± 6.7	10.4 ± 3.6	5.9 ± 2.0	−14.7 ± 2.7*§	6	5.9 ± 1.8§¥	3.7 ± 1.5	1.9 ± 0.4	−32.4 ± 6.5*¥	6
I_{tail}	29.1 ± 18.9	20.3 ± 16.5	2.5 ± 0.8	9.5 ± 6.9§	3	14.6 ± 4.9	10.1 ± 3.4	1.5 ± 0.3	38.5 ± 20.3	6
	pH_{out} 6.8					pH_{out} 6.8				
	g_{in}	g_{out}	$g_{in}:g_{out}$	V_{rev}	n	g_{in}	g_{out}	$g_{in}:g_{out}$	V_{rev}	n
I_{ss}	62.2 ± 6.4*§	9.1 ± 1.8§	9.0 ± 2.4*	2.4 ± 2.9	7	18.3 ± 5.4¥	1.2 ± 0.3*§¥	14.7 ± 1.5*	−3.5 ± 1.1*	4
I_{inst}	40.9 ± 4.9*§	11.7 ± 2.2§	4.6 ± 1.3	−12.5 ± 2.3*§	7	7.7 ± 2.5¥	3.2 ± 0.7*¥	2.4 ± 0.5	−30.0 ± 3.7*¥	4
I_{tail}	42.5 ± 6.7§	28.5 ± 5.8*	1.7 ± 0.3*	10.2 ± 8.6§	5	15.8 ± 3.6¥	11.9 ± 1.0*¥	1.3 ± 0.2	45.7 ± 17.0*	4
	pH_{out} 7.2					pH_{out} 7.2				
	g_{in}	g_{out}	$g_{in}:g_{out}$	V_{rev}	n	g_{in}	g_{out}	$g_{in}:g_{out}$	V_{rev}	n
I_{ss}	42.5 ± 8.6	27.6 ± 3.4§	1.5 ± 0.1§	−0.9 ± 0.6	2	13.5 ± 2.6§¥	1.0 ± 0.3*§¥	13.3 ± 1.0*¥	−0.4 ± 0.6	3
I_{inst}	32.6 ± 7.0	28.1 ± 3.6§	1.1 ± 0.1§	−4.0 ± 3.6§	2	6.6 ± 2.6§¥	2.9 ± 0.2*§¥	2.2 ± 0.7	−30.4 ± 6.7*¥	3
I_{tail}	38.4 ± 8.3	28.3 ± 2.4§	1.3 ± 0.2	−1.4 ± 0.6§	2	12.7 ± 1.3§¥	10.2 ± 1.5*¥	1.3 ± 0.1	55.5 ± 23.0	3

The control conditions are Bath/Pipette B1/P1.

g_{in} (nS), inward conductance; $g_{in}:g_{out}$, inward conductance (g_{in}) and the outward conductance (g_{out}) ratio; g_{out} (nS), outward conductance; I_{inst}, instantaneous current density (pA/pF); I_{ss}, steady-state current density (pA/pF); I_{tail}, instantaneous current of the deactivation current density (pA/pF); V_{rev}, reversal potential (mV); WT, wild-type.

Data is represented as mean ± SE.

*, Statistically significant differences between comparable items within the same table colum; §, statistical differences from the control pH values to other tested pH condition; ¥, statistically different values between WT and *tmem16*$^{-/-}$ mutant ($P < 0.05$).

translating into more influx or efflux of anions, respectively. A similar increase in %Rundown for all the V_m resulted in two-fold more $I_{rundown}$ compared with WT (Table 1). Interestingly, the I_{final} from both single mutants became comparable with WT values for all V_m tested. Consequently, the higher currents found in *tmem16*$^{-/-}$ and *slah3*$^{-/-}$ single mutants resulted in significantly higher inward conductivity, g_{in}, in $I_{initial}$ (Table 1). A similar trend was observed in the g_{out} from $I_{initial}$ of *tmem16*$^{-/-}$ and in *slah3*$^{-/-}$. These differences indicated that the conductivity of the remaining anionic channels present in *slah3*$^{-/-}$ and *tmem16*$^{-/-}$ might be altered to compensate for the absence of *At*SLAH3 and *At*TMEM16, either

Table 3 *Arabidopsis thaliana* Col-0 wild-type and *tmem16*$^{-/-}$ mutant current parameters under different internal pH conditions (pH_{in}), obtained immediately after entering the whole-cell configuration measured at ± 160 mV. The control conditions are Bath/Pipette B1/P1.

		WT								*tmem16*$^{-/-}$							
		pH_{in} 7.4				pH_{in} 6.8				pH_{in} 7.4				pH_{in} 6.8			
	V_m	$I_{initial}$	*N*	%RD	*n*	$I_{initial}$	*n*	%RD	*n*	$I_{initial}$	*n*	%RD	*n*	$I_{initial}$	*n*	%RD	*n*
I_{ss}	+160	365 ± 51	53	55 ± 3	53	1657 ± 280*	6	58 ± 9	6	542 ± 69$^{¥}$	24	58 ± 5	24	1157 ± 226	6	51 ± 14	6
	−160	−78 ± 11		48 ± 3		−335 ± 42		58 ± 9		−145 ± 30$^{¥}$		56 ± 5		−226 ± 28$^{¥}$		55 ± 12	
I_{inst}	+160	258 ± 38*	53	53 ± 3	53	1220 ± 199	6	53 ± 9	6	502 ± 84$^{¥}$	24	57 ± 3	24	816 ± 154$^{¥}$	6	46 ± 11	6
	−160	−89 ± 13		44 ± 3		−356 ± 42		56 ± 9		−130 ± 19$^{¥}$		54 ± 5		−258 ± 31$^{¥}$		52 ± 13	
I_{tail}	+160	400 ± 55	38	46 ± 5	31	1085 ± 186*	6	48 ± 8	4	417 ± 64	21	48 ± 6	20	787 ± 167	6	55 ± 13	5
	−160	−406 ± 50*		33 ± 4*		−766 ± 59*		57 ± 11		−462 ± 48*		37 ± 4*		−565 ± 101*$^{¥}$		26 ± 25	

	$I_{initial}$				$I_{initial}$				$I_{initial}$				$I_{initial}$			
	g_{in}	g_{out}	g_{in} : g_{out}	*n*	g_{in}	g_{out}	g_{in} : g_{out}	*n*	g_{in}	g_{out}	g_{in} : g_{out}	*n*	g_{in}	g_{out}	g_{in} : g_{out}	*n*
I_{ss}	41.4 ± 4.6§	5.4 ± 1.2	19.8 ± 2.0*§	53	88.7 ± 16.2*$^{£}$	11.4 ± 3.2$^{£}$	11.3 ± 3.5*	6	54.9 ± 7.6*§	8.7 ± 2.5	16.2 ± 2.7*	24	70.3 ± 11.5	13.6 ± 5.0	10.8 ± 3.3*	6
I_{inst}	23.2 ± 2.8*§	7.5 ± 1.4	6.3 ± 0.7*§	53	58.4 ± 9.8$^{£}$	14.8 ± 3.6$^{£}$	4.7 ± 1.2	6	31.9 ± 5.0§	9.8 ± 2.6	6.0 ± 1.1*§	24	49.3 ± 9.4	24.7 ± 8.4	3.8 ± 1.3	6
I_{tail}	32.5 ± 4.1	23.0 ± 3.2*	2.1 ± 0.3*	58	56.4 ± 11.7	29.4 ± 9.9*	2.9 ± 0.8	6	34.7 ± 5.3	22.6 ± 3.5*	1.7 ± 0.1*	21	49.7 ± 12.2	24.1 ± 18.2	1.9 ± 0.9	6

	I_{final}				I_{final}				I_{final}				I_{final}			
	g_{in}	g_{out}	g_{in} : g_{out}	*n*	g_{in}	g_{out}	g_{in} : g_{out}	*n*	g_{in}	g_{out}	g_{in} : g_{out}	*n*	g_{in}	g_{out}	g_{in} : g_{out}	*n*
I_{ss}	30.0 ± 4.7§	3.6 ± 0.8	14.8 ± 1.8*§	53	52.2 ± 16.8$^{£}$	3.7 ± 0.7$^{£}$	17.0 ± 6.2	6	28.4 ± 5.5§	4.4 ± 1.4	25.7 ± 7.6*	24	50.8 ± 16.2	10.3 ± 3.6*	9.2 ± 4.2*	6
I_{inst}	15.0 ± 2.5*§	5.5 ± 1.1	3.8 ± 0.4*§	53	29.9 ± 9.6$^{£}$	5.0 ± 1.2$^{£}$	13.0 ± 8.1	6	16.9 ± 4.2§	6.2 ± 1.6	4.7 ± 1.5*§	24	33.5 ± 10.9	17.9 ± 7.6	3.1 ± 0.8*	6
I_{tail}	23.6 ± 4.2	17.0 ± 3.5*	2.3 ± 0.5*	31	46.9 ± 19.5	30.2 ± 11.5*	1.5 ± 0.1*	4	25.9 ± 5.0	17.1 ± 3.1*	1.7 ± 0.3*	20	54.5 ± 18.8	42.1 ± 16.9*	1.4 ± 0.2*	5

	V_{rev}				V_{rev}				V_{rev}				V_{rev}			
	$I_{initial}$	*N*	I_{final}	*n*	$I_{initial}$	*n*	I_{final}	*n*	$I_{initial}$	*n*	I_{final}	*n*	$I_{initial}$	*n*	I_{final}	*n*
I_{ss}	−2.1 ± 0.7*	52	−2.0 ± 1.2*	53	0.3 ± 0.7*	6	−1.8 ± 2.3*	6	−0.6 ± 1.3*	24	0.2 ± 2.8*	24	−2.5 ± 2.1*	6	−4.3 ± 4.0*	6
I_{inst}	−15.7 ± 1.6*§	52	−23.3 ± 1.8*§	53	−6.3 ± 3.3*	6	−17.4 ± 7.9*	6	−12.6 ± 2.0*§	24	−25.8 ± 3.5*§	24	−10.3 ± 4.6*$^{£}$	6	−26.1 ± 6.6*$^{£}$	6
I_{tail}	22.7 ± 3.9*	38	27.6 ± 5.2*	31	36.2 ± 18.5*	6	31.3 ± 32.9*	4	25.6 ± 6.0*	21	35.4 ± 9.2*	20	17.4 ± 6.9*	6	39.5 ± 21.7*	5

%Inhib., percentage of inhibited current; %RD, percentage of current lost during rundown; $[NPPB]_{max}$, 5-nitro-2-(3-phenylpropylamino)benzoic acid maximum concentration tested (100 μM); g_{in} (nS), inward conductance; g_{in} : g_{out}, inward conductance (g_{in}) and the outward conductance (g_{out}) ratio; g_{out} (nS), outward conductance; I_{final}, current density (pA/pF) measured after rundown; $I_{inhibited}$, inhibited current; $I_{initial}$, initial current density (pA/pF) measured after entering whole-cell configuration; I_{inst}, instantaneous current density (pA/pF); $I_{rundown}$, current lost during rundown; I_{ss}, steady-state current density (pA/pF); I_{tail}, instantaneous current of the deactivation current density (pA/pF); V_{rev}, reversal potential (mV); WT, wild-type.
Data is represented as mean ± SE.
*, Statistically significant differences between comparable parameters within the same table column; $^{¥}$, statistical significantly differences between wild-type and *tmem16*$^{-/-}$ mutant; §, statistical differences between comparable parameters in the initial and final current; $^{£}$, statistical differences between parameters obtained in pH_{in} = 7.4 (WT) and pH_{in} = 6.8 ($P < 0.05$).

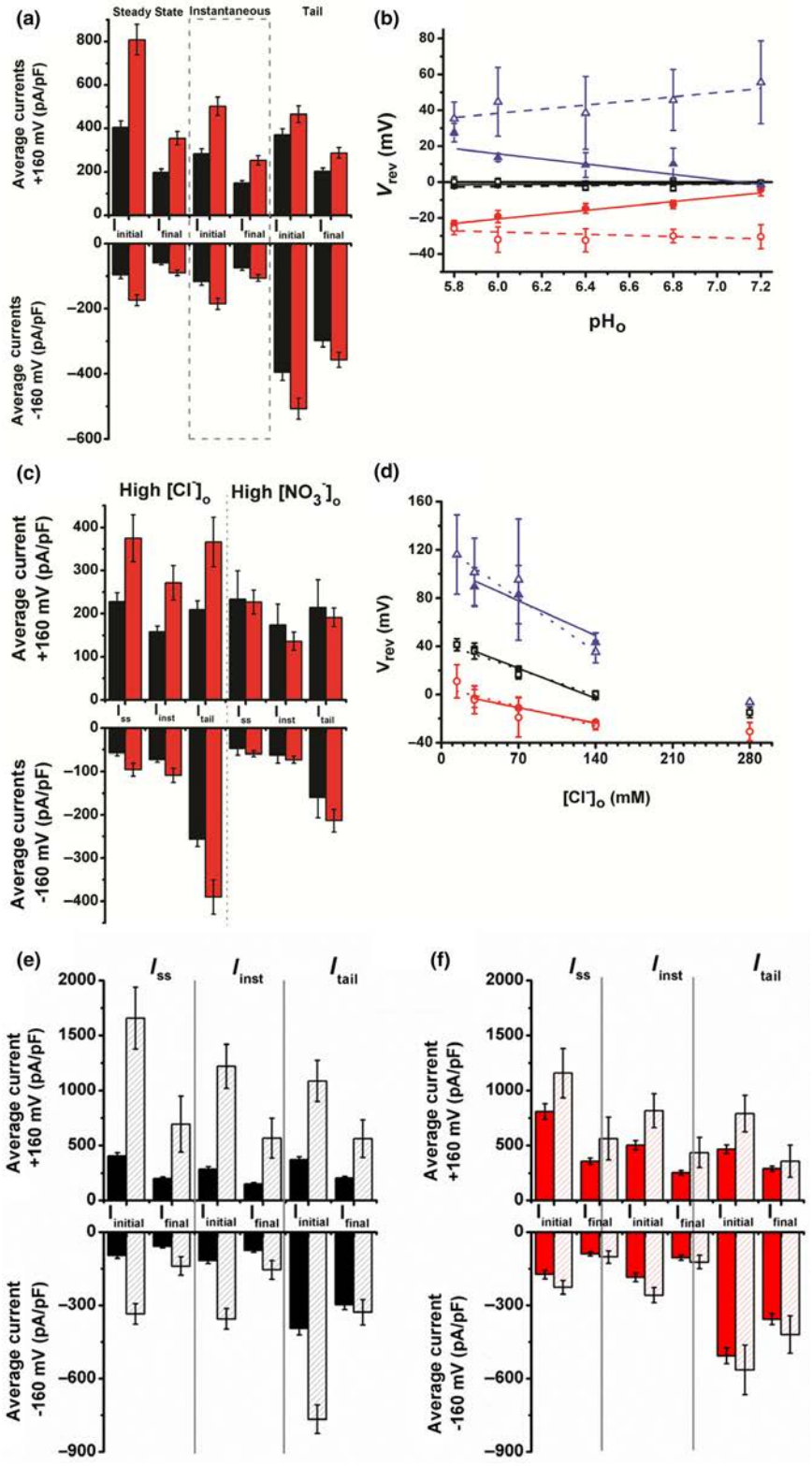

by displaying more conductivity than those present in WT, hinting at a possible regulatory role, or by ion compensation. In other words, in WT protoplasts the bulk current generated by *At*SLAH3 and *At*TMEM16 channels would translate into less influx in the presence of *At*SLAH3 and less influx and efflux in the presence of *At*TMEM16, respectively. When negative V_m were applied, *almt12*$^{-/-}$ protoplasts showed a reduction of 32% I_{final} for the negative V_m (less efflux) compared with WT protoplasts (Table 1). This result suggests that *At*ALMT12 channels may be contributors to the global ion

Fig. 2 *Arabidopsis thaliana* averaged normalised (pA/pF) steady-state whole-cell (WC) anionic currents elicited with the activation protocol and Bath/Pipette B1/P1 solutions. (a) Wild-type (WT) (black) and *tmem16*$^{-/-}$ mutant (red) average current amplitude for the currents before and after rundown ($I_{initial}$ and I_{final}) at ± 160 mV for all three current properties (steady state, instantaneous and tail). (b) Reversal potentials (V_{rev}) under different external pH (pH_{out}) for steady state (squares, WT; open squares, *tmem16*$^{-/-}$), instantaneous (circles, WT; open circles, *tmem16*$^{-/-}$) and tail (triangles, WT; open triangles, *tmem16*$^{-/-}$) currents (I_{final}, control condition is at pH_{out} 5.8). Lines represent the linear fit for the V_{rev} for each current property. Data points from pH_{out} 5.6 were not used for the fitting. (c) *Arabidopsis thaliana* WT (black) and *tmem16*$^{-/-}$ mutant (red) average current amplitude for I_{final} under external high $[Cl^-]$ ($[Cl^-]_{out}$) and high external $[NO_3^-]$ ($[NO_3^-]_{out}$) conditions (P1/B1 to B4), measured at ± 160 mV for all three current properties. (d) *Arabidopsis thaliana* WT and *tmem16*$^{-/-}$ mutant V_{rev} under different $[Cl^-]_{out}$ for steady state (squares, WT; open squares, *tmem16*$^{-/-}$), instantaneous (circles, WT; open circles, *tmem16*$^{-/-}$) and tail (triangles, WT; open triangles, *tmem16*$^{-/-}$) currents (I_{final}, control condition is $[Cl^-]_{out}$ = 140 mM). Lines represent the linear fit for the V_{rev} for each current property. Data points from $[Cl^-]_{out}$ = 280 mM were not used for the fitting. (e, f) Average current amplitude comparison between all three current properties, I_{ss} (steady state), I_{inst} (instantaneous), and I_{tail} (tail) before ($I_{initial}$) and after rundown (I_{final}), for Arabidopsis WT (black) and *tmem16*$^{-/-}$ mutant (red) between the control condition (pH_{in} 7.2; full columns) and internal acidic pH condition (pH_{in} 6.8; open columns). Data are represented as mean ± SE. All the results shown were obtained with the first allele, but the pH insensitivity phenotype was determined to be reproducible on the second allele (Supporting Information Fig. S2).

conductivity in the negative V_m range tested, along with *At*SLAH3 channels.

The double mutant *almt12*$^{-/-}$; *slah3*$^{-/-}$ was used to investigate possible synergistic effects on currents (Table 1). $I_{initial}$ and I_{final} for the negative V_m were found to show reductions of 37% and 61% (less efflux) when compared with *almt12*$^{-/-}$, 37% and 73% when compared with WT, and 64% and 77% when compared with *slah3*$^{-/-}$ mutant. These results depicted a decrease in the net current at physiological potentials compatible with the idea that both *At*ALMT12 and *At*SLAH3 are the main generators of the efflux produced in this range. Strikingly, $I_{initial}$ for positive V_m did not differ in the double mutant in relation to WT and *almt12*$^{-/-}$. As a consequence, %Rundown in *almt12*$^{-/-}$;*slah3*$^{-/-}$ was much higher for negative V_m, and the $g_{in} : g_{out}$ ratio was also significantly higher, resulting in stronger effluxes after rundown, relative to the positive V_m range (81 ± 19 vs 14.8 ± 1.8 WT vs 31 ± 7 *almt12*$^{-/-}$; Table 1). Interestingly, V_{rev} from $I_{initial}$ in *almt12*$^{-/-}$;*slah3*$^{-/-}$ was close to the one obtained for the single *slah3*$^{-/-}$. This result together with the reduced $I_{initial}$, I_{final} and respective conductance (Table 1) observed again suggests that both channels are major contributors to the overall current.

After rundown, 100 μM NPPB was added to *almt12*$^{-/-}$; *slah3*$^{-/-}$ protoplasts. The $I_{inhibited}$ obtained for all V_m tested was significantly different than WT (−160 mV: −1 ± 0.4 vs −26 ± 21 pA/pF, +160 mV: 11.9 ± 2.9 vs 53 ± 10, respectively) and slightly higher when compared with the singles *slah3*$^{-/-}$ and *almt12*$^{-/-}$ (−160 mV: −2.6 ± 3.2 and −4 ± 2 pA/pF, respectively; Table 1). Interestingly, *tmem16*$^{-/-}$ showed a significant reduction of sensitivity to NPPB for all applied V_m (−160/+160 mV, −1.7 ± 0 and 13 ± 10 pA/pF, respectively; Table 1). The lack of inhibition in the double mutant, as seen in the single mutants, particularly at the physiological potentials, implies that AtTMEM16A, *At*SLAH3 and partly AtALMT12 conducted the bulk of the NPPB inhibited current fraction. In other words, these channels are likely to be the most affected by the NPPB treatment.

Taken together, the results strongly suggested that *At*ALMT12, *At*SLAH3 and, to a lesser extent, *At*TMEM16A channels are major contributors of the current measured at physiological potentials. At the cellular level, this would implicate that all three channels are responsible for the anionic efflux at the plasma membrane (PM) of Arabidopsis hydrated pollen protoplasts.

*At*TMEM16 is an anion/H^+ symporter

Alkalinisation of the bath solution (pH 5.8–7.2, B1/P1 in Table S2) induced major changes in current amplitude, rectification and a major shift in the V_{rev} for the instantaneous currents (Table 2, Fig. S2). We defined I_{inst} and I_{tail} as transient currents, and their full description is available in Methods S6. While the V_{rev} for I_{ss} (steady-state current) always remains very close to the predicted E_{Cl^-}, the V_{rev} of the transient currents (I_{inst} and I_{tail}) shifts towards E_{Cl^-} as the H^+ gradient across the membrane is reduced, equalising E_{H^+} to E_{Cl^-} (Tables 2, S3, Fig. 2b). These differences are evidence of a transient H^+ current permeating the membrane in the immediate moments after a voltage jump. Together with results from decreased $[Cl^-]_{out}$ experiments (Fig. 1j–l; Table 4), the presence of a cotransporter becomes self-evident after observation of the sub-Nernstian V_{rev} shift along with the V_{rev} H^+ dependency of the instantaneous currents seen here (Fig. 2b).

The *tmem16*$^{-/-}$ mutant shows a very subtle phenotype under patch-clamp control conditions (B1/P1) compared with WT (Tables 1–3, Fig. 2a). However, upon changing extracellular pH (pH_{out}) a drastic difference emerges (Fig. 2b, Table 2). Contrary to WT, in which pH_{out} increase leads to an almost complete loss of rectification and overall current amplitude significantly increases (Fig. S2a–f), in *tmem16*$^{-/-}$ no changes in currents were observed in response to pH_{out} (Fig. S2g–l). A second allele shows a similar electrophysiological profile (Fig. S2m–o). Hence, despite showing larger current amplitudes in the control pH_{out} condition (Fig. 2a, Table 2), the *tmem16*$^{-/-}$ anionic currents do not respond to pH changes (Fig. S2g–l). Furthermore, the respective shifts in V_{rev} for the transient currents (I_{inst} and I_{tail}) to increasing pH_{out} are abolished (Fig. 2b). These observations further supported the hypothesis of an H^+/anionic cotransporter system mediated by *At*TMEM16. The increase in current intensity observed in the *tmem16*$^{-/-}$ mutants is an indication that *At*TMEM16 is transporting Cl^- against its electrochemical gradient, creating smaller overall anionic currents in WT pollen protoplasts. In relation to the initial shift of V_{rev} from E_{Cl^-} observed in the transient currents, in both WT and *tmem16*$^{-/-}$ mutants, it is plausible that these could be accounted for by an H^+ current, which fails to be rectified in the absence of *At*TMEM16 under alkaline pH. Based on the slopes for the V_{rev} shifts under different

Table 4 Current parameters for *Arabidopsis thaliana* wild-type and *tmem16*$^{-/-}$, under different external [Cl^-] or [NO_3^-] concentrations.

	WT					*tmem16*$^{-/-}$				
	$[Cl^-]_{out}$ = 14 mM					$[Cl^-]_{out}$ = 14 mM				
	g_{in}	g_{out}	$g_{in} : g_{out}$	V_{rev}	n	g_{in}	g_{out}	$g_{in} : g_{out}$	V_{rev}	n
I_{ss}	–	–	–	–	–	7.7 ± 3.3§	1.8 ± 0.8	6.3 ± 4.5	41.3 ± 5.0§	2
I_i	–	–	–	–	–	4.4 ± 1.2§	2.7 ± 0.4§	1.8 ± 0.7	10.9 ± 13.6§	2
I_t	–	–	–	–	–	9.8 ± 0.3§	7.9 ± 0.4*§	1.3 ± 0.1	116.0 ± 33.0§	2
	$[Cl^-]_{out}$ = 30 mM					$[Cl^-]_{out}$ = 30 mM				
	g_{in}	g_{out}	$g_{in} : g_{out}$	V_{rev}	n	g_{in}	g_{out}	$g_{in} : g_{out}$	V_{rev}	n
I_{ss}	5.1 ± 2.2§	0.4 ± 0.1§	10.7 ± 3.8	36.9 ± 3.1*§	7	12.6 ± 4.7	1.0 ± 0.6§	35.9 ± 22.4	36.0 ± 6.7§	3
I_i	3.4 ± 1.8§	0.6 ± 0.2$^{\S¥}$	4.2 ± 1.2	−3.2 ± 7.5*§	7	4.5 ± 1.6*§	2.2 ± 0.5$^{\S¥}$	2.1 ± 0.6	−4.5 ± 11.5*	3
I_t	4.3 ± 1.7$^{\S¥}$	4.0 ± 2.5§	1.7 ± 0.4	89.5 ± 15.8*§	7	11.6 ± 1.3$^{\S¥}$	8.4 ± 0.6*§	1.4 ± 0.2	101.3 ± 28.3§	3
	$[Cl^-]_{out}$ = 70 mM					$[Cl^-]_{out}$ = 70 mM				
	g_{in}	g_{out}	$g_{in} : g_{out}$	V_{rev}	n	g_{in}	g_{out}	$g_{in} : g_{out}$	V_{rev}	n
I_{ss}	8.9 ± 0.4§	0.6 ± 0.3§	21.9 ± 8.2	20.5 ± 3.1*§	3	12.1 ± 7.8	1.0 ± 0.7§	29.8 ± 27.3	16.6 ± 3.8	2
I_i	3.9 ± 0.9*§	1.1 ± 0.5§	5.5 ± 2.2	−11.2 ± 9.0*	3	5.1 ± 2.1§	2.3 ± 0.2§	2.4 ± 1.1	−19.2 ± 16.3	2
I_t	8.5 ± 1.4§	4.4 ± 1.9§	2.2 ± 0.7	82.9 ± 24.2*	2	12.5 ± 2.5§	9.7 ± 0.1*§	1.3 ± 0.2	95.3 ± 50.3	2
	$[Cl^-]_{out}$ = 140 mM					$[Cl^-]_{out}$ = 140 mM				
	g_{in}	g_{out}	$g_{in} : g_{out}$	V_{rev}	n	g_{in}	g_{out}	$g_{in} : g_{out}$	V_{rev}	n
I_{ss}	30.0 ± 4.7	3.6 ± 0.8	14.8 ± 1.8*	−2.0 ± 1.2*	53	28.4 ± 5.5	4.4 ± 1.4	25.7 ± 7.6*	0.2 ± 2.8*	24
I_i	15.0 ± 2.5*	5.5 ± 1.1	3.8 ± 0.4*	−23.3 ± 1.8	53	16.9 ± 4.2	6.2 ± 1.6	4.7 ± 1.5*	−25.8 ± 3.5*	24
I_t	23.6 ± 4.2	17.0 ± 3.5*	2.3 ± 0.5*	27.6 ± 5.2*	31	25.9 ± 5.0	17.1 ± 3.1*	1.7 ± 0.3*	35.4 ± 9.2*	20
	$[Cl^-]_{out}$ = 280 mM					$[Cl^-]_{out}$ = 280 mM				
	g_{in}	g_{out}	$g_{in} : g_{out}$	V_{rev}	n	g_{in}	g_{out}	$g_{in} : g_{out}$	V_{rev}	n
I_{ss}	–	–	–	–	–	17.4 ± 9.7	7.6 ± 6.9	7.1 ± 5.2	−14.9 ± 4.4	2
I_i	–	–	–	–	–	9.9 ± 5.7	8.0 ± 7.3	3.7 ± 2.7	−30.8 ± 7.5	2
I_t	–	–	–	–	–	22.6 ± –	18.3 ± –	1.2 ± –	−6.4 ± –	1
	$[NO_3^-]_{out}$ = 140 mM					$[NO_3^-]_{out}$ = 140 mM				
	g_{in}	g_{out}	$g_{in} : g_{out}$	V_{rev}	n	g_{in}	g_{out}	$g_{in} : g_{out}$	V_{rev}	n
I_{ss}	10.3 ± 4.0§	1.1 ± 0.5	14.9 ± 3.8*	−4.1 ± 8.0*	8	41.4 ± 3.6$^{\S¥}$	8.0 ± 1.8$^{¥}$	5.6 ± 1.1*$^{\S¥}$	1.2 ± 3.2*	3
I_i	5.8 ± 2.2§	1.5 ± 0.5§	4.0 ± 0.6	−18.4 ± 11.4*	8	17.7 ± 3.0*$^{¥}$	10.0 ± 2.6$^{¥}$	1.9 ± 0.3	−21.4 ± 3.3*	3
I_t	8.8 ± 4.0§	4.0 ± 2.3§	2.7 ± 0.4	10.9 ± 3.0*§	6	29.8 ± 1.2$^{¥}$	23.8 ± 1.0*$^{¥}$	1.2 ± 0.0	12.8 ± 3.4*§	3

The control conditions are Bath/Pipette B1/P1 ($[Cl^-]_{out}$ = 140 mM). The different external [Cl^-] ($[Cl^-]_{out}$) were obtained with solutions B6–B9. $[NO_3^-]_{out}$ stands for currents elicited with high [NO_3^-] in the bath solution (B4).

g_{in} (nS), inward conductance; $g_{in} : g_{out}$, inward conductance (g_{in}) and the outward conductance (g_{out}) ratio; g_{out} (nS), outward conductance; I_{inst}, instantaneous current density (pA/pF); I_{ss}, steady-state current density (pA/pF); I_{tail}, instantaneous current of the deactivation current density (pA/pF); V_{rev}, reversal potential (mV); WT, wild-type.

Data are represented as mean ± SE.

*, Statistically significant differences between comparable items within the same table column; §, statistical differences between comparable items in the initial and final current; ¥, $P < 0.05$ statistically different values between WT and *tmem16*$^{-/-}$ mutant.

pH_{out} and $[Cl^-]_{out}$ in the WT I_{inst} (Fig. 2b,d), we can estimate a $2H^+ : 1A^-$ stoichiometry for the *At*TMEM16 H^+/anion cotransporter. We expect that H^+ are being transported along their electrochemical gradient (created *in vivo* by the H^+-ATPase) that energises the cotransporter, allowing it to transport anions against their electrochemical gradient. Furthermore, we observed that as the H^+ electrochemical gradient across the PM diminishes (pH_{in} = 7.2 and pH_{out} changing from 5.6 to 7.2), the current increases in intensity and loses its rectification. These results strongly suggested that *At*TMEM16 is an H^+/Anion symporter.

Table 5 *Arabidopsis thaliana* anion current parameters calculated for wild-type and for the mutant line *almt12*$^{-/-}$ obtained in Bath/Pipette B1/P1 solutions measured at ± 160 mV, in the presence of GABA or Muscimol.

	WT + 500 μM GABA				WT + 10 μM Muscimol				*almt12*$^{-/-}$ + 10 μM Muscimol			
	$I_{(-160\ mV)}$	$I_{(+160\ mV)}$	V_{rev}	*n*	$I_{(-160\ mV)}$	$I_{(+160\ mV)}$	V_{rev}	*n*	$I_{(-160\ mV)}$	$I_{(+160\ mV)}$	V_{rev}	*n*
$I_{initial}$	−12 ± 2.6¥	217 ± 38¥	4.8 ± 1.4	5	−21 ± 3¥	207 ± 47¥	4 ± 0.2	5	−84 ± 21	398 ± 40	−3 ± 2.4	5
I_{final}	−3 ± 0.5¥	46 ± 6¥	1.9 ± 0.6	5	−10 ± 4.7¥	65 ± 23¥	4 ± 1	4	−33 ± 13	204 ± 45	−2.5 ± 2.1	4
$I_{rundoewn}$	−8.7 ± 3.5	154 ± 38¥	3.2 ± 1.9¥	5	−20 ± 12¥	78 ± 11¥	1.8 ± 2¥	4	−54 ± 11	195 ± 23	5 ± 1.9	4
$I_{inhibited}$	−0.32 ± 0.4¥	5.5 ± 3.7¥	−0.3 ± 0.2¥	3	−3 ± 1.6¥	1.04 ± 0.9¥	0.7 ± 0.2¥	3	9.8 ± 3¥	51.5 ± 16	−2 ± 1.2	4
%RD	74 ± 4¥	75 ± 3¥		5	72 ± 7¥	41 ± 15		4	61 ± 7	49 ± 7		13
%Inhib.	20 ± 8.5¥	21 ± 9		3	11 ± 2¥	9.3 ± 1¥		3	29 ± 10¥	25 ± 13		4

	g_{in}	g_{out}	$g_{in} : g_{out}$	*n*	g_{in}	g_{out}	$g_{in} : g_{out}$	*n*	g_{in}	g_{out}	$g_{in} : g_{out}$	*n*
$I_{initial}$	21 ± 0.3¥	7 ± 0.01¥	29.7 ± 5.7	5	20.9 ± 0.45¥	2 ± 0.05¥	13 ± 4.5	5	35 ± 0.9	4.4 ± 0.2	11.3 ± 8.7	5
I_{final}	14 ± 0.14¥	3 ± 0.005¥	59 ± 8¥	5	10.5 ± 0.4¥	1 ± 0.04¥	11 ± 3¥	4	28 ± 0.5	1.2 ± 0.04¥	25 ± 3.5	4
$I_{rundoewn}$	14 ± 0.33	0.6 ± 0.02¥	24 ± 3¥	5	6 ± 0.3¥	2 ± 0.05	4.6 ± 2.5	4	21 ± 0.6	3 ± 0.1	9.5 ± 4	4
$I_{inhibited}$	0.05 ± 0.06¥	0.003 ± 0.008¥	9.5 ± 2.4¥	3	1.3 ± 0.9	0.07 ± 0.03	19.5 ± 11.7	3	0.4 ± 0.2	-	-	3

%Inhib., percentage of inhibited current; %RD, percentage of current lost during rundown; $[NPPB]_{max}$, 5-nitro-2-(3-phenylpropylamino)benzoic acid maximum concentration tested (100 μM). GABA, γ-aminobutyric acid; g_{in} (nS), inward conductance; $g_{in} : g_{out}$, inward conductance (g_{in}) and the outward conductance (g_{out}) ratio; g_{out} (nS), outward conductance; I_{final}, current density (pA/pF) measured after rundown; $I_{inhibited}$, inhibited current density (pA/pF); $I_{initial}$, initial current density (pA/pF) measured after entering whole-cell configuration; $I_{rundown}$, current density (pA/pF) lost during rundown; V_{rev}, reversal potential (mV); WT, wild-type.

Data are represented as mean ± SE.

¥ and δ, $P < 0.05$ refer to significant differences between comparable elements of different experimental groups between WT and *almt12*$^{-/-}$, respectively (both values are depicted in Table 1).

We then tried to establish TMEM16 ionic specificity. In WT the anionic selectivity experiments showed a preference for NO_3^- over Cl^- (Tables S2, S5, Fig. 1d–i), but without a significant change in current intensity. This was not the case for the currents in *tmem16*$^{-/-}$ mutants. The increase in current amplitude observed in *tmem16*$^{-/-}$ in control conditions was abolished when $[Cl^-]$ was substituted for $[NO_3^-]$ on the external bath, restoring the mutant current amplitude to values identical to WT (Table 4; Fig. 2c). This result suggested that TMEM16 is more selective for Cl^- over NO_3^-.

The effect of internal pH (pH_{in}) was also investigated. We observed a strong regulation on the anionic currents mediated by pH_{in} in both WT and *tmem16*$^{-/-}$ (Table 3, Fig. 2e–f). These results showed an increase in current amplitude by acidic pH_{in} in WT that is impaired in the *tmem16*$^{-/-}$ mutant. This finding indicated that pH_{in} also modulates the anionic currents through the activity of *At*TMEM16, although to a lesser extent than that of pH_{out}. Pollen competition assays in heterozygous *tmem16*$^{+/-}$ mutant plants resulted in a subtle, but significant, loss of fitness (Fig. S3).

*At*ALMT12 is modulated by GABA

GABA may act as an upstream effector of anion-driven PT growth. This hypothesis emerged from the recent finding that the aluminium-activated malate transporter (ALMT) protein family is regulated by this amino acid, and from the fact that PTs of *A. thaliana* were affected by GABA-specific pharmacology (Ramesh *et al.*, 2015). Here we sought to test this hypothesis through genetics. We first applied the patch-clamp technique to WT and *almt12*$^{-/-}$ mutant pollen protoplasts in the presence of different GABA concentrations and muscimol (a universal agonist for all GABA type A receptors ($GABA_A$), with 3–11 times greater affinity for GABA-binding sites than GABA itself; (Krogsgaard-Larsen & Johnston, 1978; Nicholson *et al.*, 1979). GABA addition to the bath solution had no effect on the overall anionic currents. However, addition of 500 μM of GABA ($n = 5$) or 10 μM muscimol ($n = 5$) to the intracellular medium (B1/P1; Table S2), induced a 50% decrease in the $I_{initial}$ and I_{final}, and up to a 90% decrease in the $I_{initial}$ and I_{final} (Fig. S4a,c,d), within 5–10 min, resulting in a significant loss of channel conductivity in all V_m tested (Table 5; Fig. 3a).

The fact that *At*ALMT12 shares the GABA-binding motif with the ALMT family and the $GABA_A$ receptor (Fig. S5), suggested that GABA and muscimol are inhibiting part of the WT current by acting on *At*ALMT12. Because muscimol had a strong effect on the anionic currents, 10 μM was added to the pipette solution in *almt12*$^{-/-}$ mutant protoplasts ($n = 4$). Strikingly, its effect was completely abrogated on the mutant and the properties of the currents were similar to those in *almt12*$^{-/-}$ mutants without muscimol treatment (Tables 1, 5; Figs 3b, S4b,d). We therefore hypothesised that, at a macroscopic level, growth rate should behave equally. Fig. 3(c) confirms this assumption, as PTs from two independent alleles of *almt12*$^{-/-}$ became insensitive to muscimol, while in WT this drug significantly inhibited PT growth. To further gain insight into the possible interplay between GABA and *At*ALMT12 channels, heterologous expression of the protein was performed in the mammalian cell line COS-7. The *At*ALMT12-transfected cells produced voltage-dependent inward currents that resembled the *At*ALMT12 electrophysiological profile previously described (Meyer *et al.*, 2010) (MB1/MP1; Fig. 3d–f). The GABA effect on *At*ALMT12 was

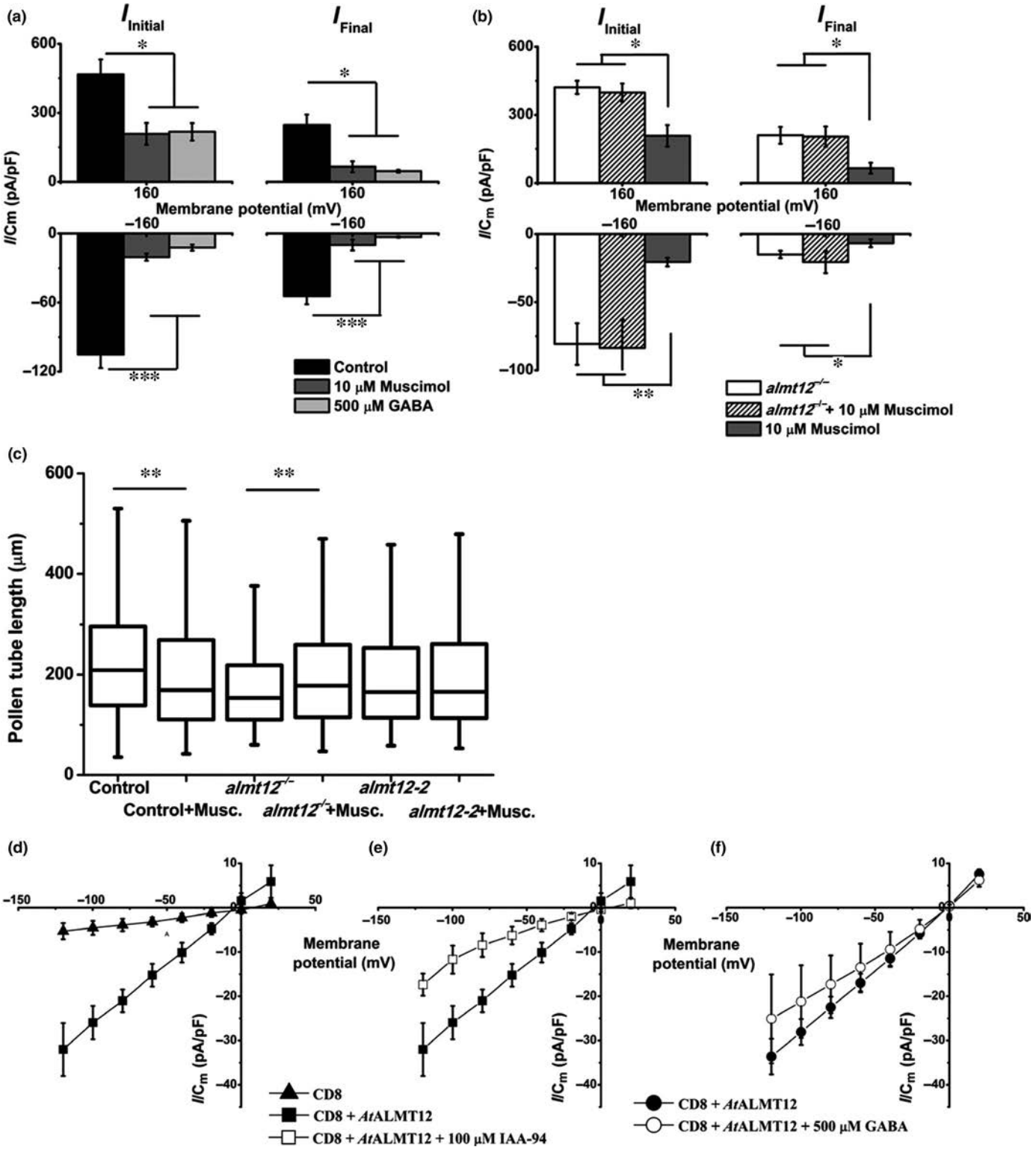

observed when 500 μM were applied to the extracellular solution, namely current reduction (Table 5; Fig. 3c–e). These results corroborated previous results (Ramesh *et al.*, 2015) and implied that muscimol, hence GABA, regulates PT growth via *At*ALMT12 channels.

Pollen tubes from *ccc*$^{-/-}$ and *slah3*$^{-/-}$ mutants show reduced apical anion effluxes

We have previously described the extracellular net anion fluxes for lily, tobacco, and Arabidopsis PTs (Zonia *et al.*, 2002;

Fig. 3 The effect of γ-Aminobutyric acid (GABA) in whole-cell (WC) anionic currents acquired from *Arabidopsis thaliana* pollen protoplasts and in COS-7 mammalian cells transfected with *At*ALMT12. (a, b) Averaged normalised (pA/pF) steady-state anionic currents using Bath/Pipette B1/P1 solutions. Current acquired 10 min after entering WC configuration ($I_{initial}$), and after rundown (I_{final}), measured at ± 160 mV. Data are represented as mean ± SE. *, $P < 0.05$; ***, $P < 0.001$. (a) Comparison between control/wild-type (WT; $n = 6$), $[500\ \mu M]_{in}$ GABA ($n = 5$) and $[10\ \mu M]_{in}$ muscimol ($n = 5$), added to the pipette solution. (b) Currents from the mutant *almt12*$^{-/-}$ in the absence ($n = 5$) or presence of $[10\ \mu M]_{in}$ muscimol ($n = 4$). Currents acquired from WT protoplasts with muscimol are also depicted for comparison. (c) *A. thaliana* pollen tube length measurements collected in the absence and presence of 20 μM muscimol from the WT ($n = 1518$ and $n = 1614$, respectively), from the *almt12*$^{-/-}$ mutant line ($n = 1068$ and $n = 1067$, respectively), and from a second *At*ALMT12 independent mutant line (*almt12-2*, $n = 1061$ and $n = 1648$, respectively), measured with the anion-selective self-referencing probe. The presence of muscimol induce tube growth inhibition in the WT but not in the two mutant *almt12*$^{-/-}$ lines. Data are represented as mean ± SE. **, $P < 0.01$. (d–f) Transient transfection analysis in the mammalian cell line COS-7 acquired after 72 h posttransfection with CD8 Dynabeads + *At*ALMT12. Current−voltage (*I*/*V*) curves obtained from the average normalised (pA/pF) steady-state (last 50 ms) currents elicited with MB1/MP1 solutions in a series of 1 s voltage jumps that ranged between −120 and +100 mV, after a prepulse of +40 mV are depicted. (d) *I*/*V* curve obtained from CD8 alone (triangles, $n = 6$) or CD8 + *At*ALMT12 (squares, $n = 6$) transfected cells. (e) *I*/*V* curve obtained from cells transfected with CD8 + *At*ALMT12, before (squares, $n = 6$) and after (open squares, $n = 3$) the application of 100 μM of Indanyloxyacetic acid 94 (IAA-94), a potent Cl^- channel blocker to the bath solution. (f) *I*/*V* curve obtained before (CD8 + *At*ALMT12, circles) and after applying 500 μM GABA to the extracellular solution (open circles, $n = 3$). Data are represented as mean ± SD.

Gutermuth *et al.*, 2013). Using a non-invasive, anion-specific vibrating probe, we expanded this analysis to single, and double mutants of the anionic transporter candidates, and their respective growth rate (Fig. 4a,b). Growth rate, depicted in Fig. 4(a), was significantly affected in all mutants bearing the *ccc* mutation (*ccc*$^{-/-}$ and *tmem16*$^{-/-}$;*ccc*$^{-/-}$). Homozygous plants for a second independent T-DNA insertion in the *CCC* gene exhibited a similarly reduced growth rate (Fig. S6). The impaired growth rate obtained for both *CCC* mutant insertion lines may explain the development of shorter siliques and the reduced seed set (Colmenero-Flores *et al.*, 2007).

Conversely, the *ccc*$^{-/-}$ and *slah3*$^{-/-}$ mutants, showed anionic effluxes that were significantly lower at the tip compared with WT PTs, while *almt12*$^{-/-}$ and *tmem16*$^{-/-}$ were not affected (Fig. 4b). Counterintuitively, the anion fluxes measured in the double mutant *tmem16*$^{-/-}$;*ccc*$^{-/-}$ are comparable with WT, presenting a significant recovery in comparison with the single mutant *ccc*$^{-/-}$, but not from *tmem16*$^{-/-}$. Similarly, the anion fluxes of the double mutant *almt12*$^{-/-}$;*slah3*$^{-/-}$ were comparable with WT, and significantly higher than *slah3*$^{-/-}$. The flux data should be interpreted in light of the knowledge that these extracellular probes report the sum of all currents in a given membrane domain. Nevertheless, the elevated anion fluxes observed in both double mutants (*tmem16*$^{-/-}$;*ccc*$^{-/-}$ and *almt12*$^{-/-}$;*slah3*$^{-/-}$) revealed the existence of functional compensations of the same kind found within the GLUTAMATE RECEPTOR-LIKE channel family, that we could partially explain by compensation of intracellular compartments where some of the channels are located (Wudick *et al.*, 2018). We therefore further characterised the location of the anion channels analysed.

SLAH3 is localised in the shank and at the tip of the PTs, while CCC is present only at the shank

Given the striking polarisation of anionic fluxes and cytosolic Cl^- concentration in PTs (Zonia *et al.*, 2002; Gutermuth *et al.*, 2013) we looked into the localisation of the four anion transporters in PTs by generating GFP chimeras under the pollen-specific promoter LAT52. Confocal imaging of transgenic lines for the *At*CCC transporter (Fig. 4c) showed a preferential allocation to the shank of the PT and grain, decreasing to a more diffuse signal up to the subapical area, but not reaching the tip (black arrow in c). The pattern of distribution changes along the length of the tube, from clear location on the PM (transect a–a′ on Fig. 4c), to mostly cytoplasmic towards the subapical area (c–c′) and a transition zone (b–b′) where labelling is still observable on the PM. Profiles for these transects (Fig. 4e) clearly show this change, from two clearly visible peaks on the cell boundaries (a–a′) that become almost indistinguishable at the tip-proximal zone (c–c′). The insert on Fig. 4(c) corresponds to a forming callose plug (boxed area) and confirms the nature of the labelling in the PM on the tip-distal areas by two criteria as the labelling: (1) contours perfectly the plug constriction, showing that it is not on the cell wall; and (2) is clearly visible in the nascent stretches of membrane (white arrows) that will seal the two segments of the tube. This pattern around the callose plug is exactly like the one described for the *bona fide* PM H^+-ATPase *Nt*AHA1 (Certal *et al.*, 2008). Yet, in the most tip-proximal zones, cytoplasmic labelling was clearly observed, sometimes with a particulate morphology. We therefore resorted to more sensitive widefield imaging (Fig. 4d). Despite less resolution on the *z*–*z*′ axis due to the absence of optical slicing, even on shorter PTs, PM labelling can still be resolved near the PG (transect d–d×, profile in Fig. 4e, asterisks corresponding to PM), and this pattern was confirmed upon double-labelling with FM 4-64 dye (Fig. 4d). Yet in the tip-proximal zones, PM labelling was no longer resolvable and, along the whole tube, an increase in cytoplasmic labelling was observed, sometimes with a particulate nature that could be interpreted as the Golgi/*trans*-Golgi network previously described (Henderson *et al.*, 2015). *At*SLAH3–GFP was observed to have a clear location on the PM, more intense on the shank and less intense on the tip (Fig. 4f). Interestingly, it seems that in the *At*SLAH3–GFP protein, fusion was being constantly carried and delivered by an intense movement of vesicles along the PT's cytoplasmic streaming (Video S1). Similar to *At*CCC−GFP lines, *At*TMEM16−GFP PTs also depicted a signal at the shank and no signal at the tip, but without clear PM localisation. Video S2 shows distribution of the fusion protein along membranous structures that resembled elongated stretched vacuoles. The fact that a clear PM was not observed and that there were

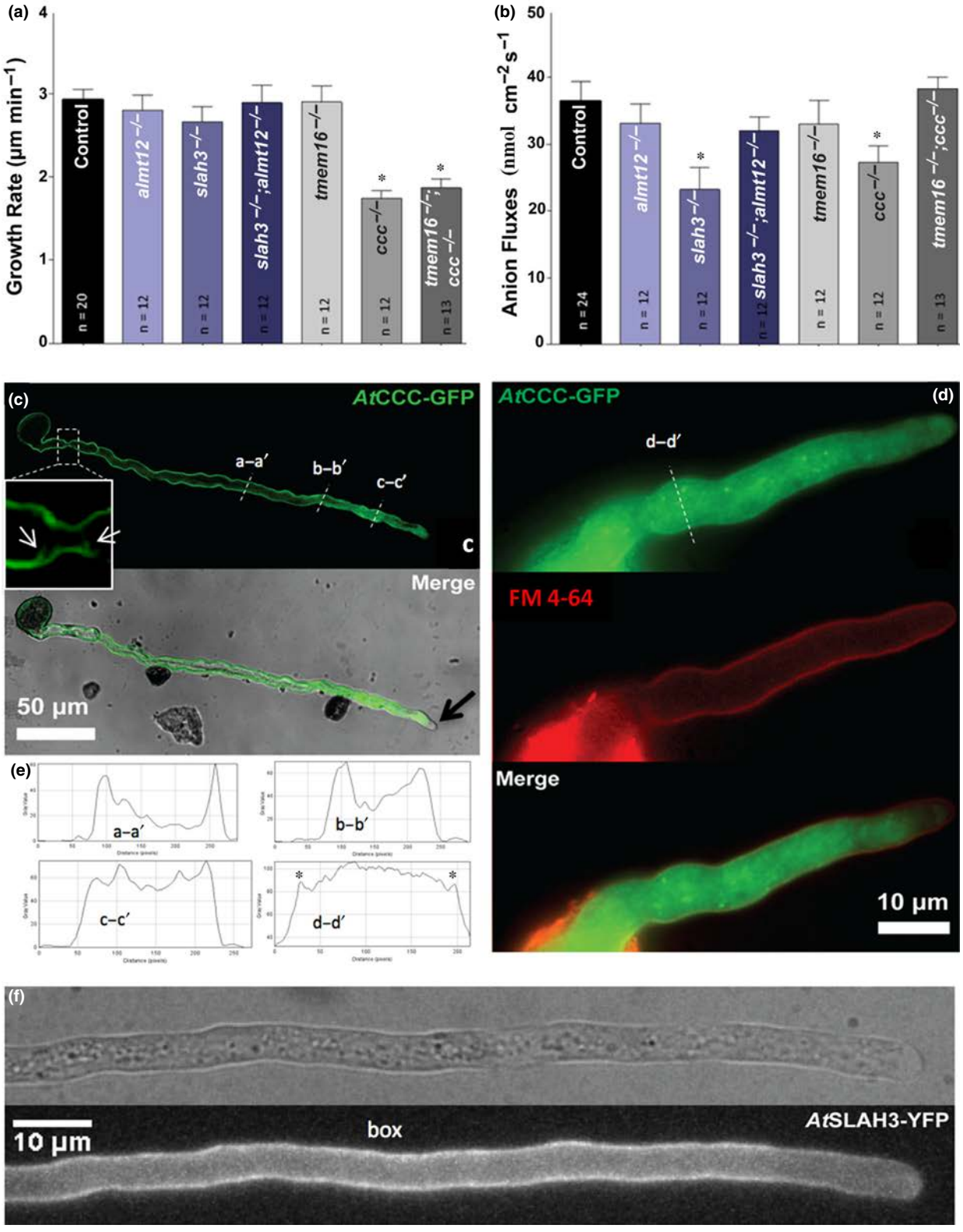

variations between lines using C- and N- terminal fusion of GFP raised doubts if these images can be interpreted as the final location or trafficking accumulation, a recurring problem with many low expression level PM channels. Likewise, the *At*ALMT12–GFP lines presented a vesicle localisation similar to the one seen with SLAH3 protein, but without a clear PM localisation (Fig. S7). Again, this protein showed considerable variation between different transformed lines and C- and

Fig. 4 (a, b) Growth rate and anion fluxes measured in *Arabidopsis thaliana* wild-type (WT) pollen tubes (PTs) ($n = 24$), *almt12*$^{-/-}$ ($n = 12$), *slah3*$^{-/-}$ ($n = 12$), *almt12*$^{-/-}$;*slah3*$^{-/-}$ ($n = 12$), *tmem16*$^{-/-}$ ($n = 12$), *ccc*$^{-/-}$ ($n = 12$), and *tmem16*$^{-/-}$;*ccc*$^{-/-}$ ($n = 13$). Data are represented as mean ± SE. *, $P < 0.05$ refers to significant differences between comparable elements in the same experimental group. (c–e) Fluorescence imaging of transgenic PTs overexpressing *At*CCC-GFP. (c) Overexpression of *At*CCC-GFP reveals the presence of the transporter at the plasma membrane (PM), with preferential allocation to the shank of the PT and grain with a decreasing and more diffuse signal up to the subapical area, but not reaching the tip (black arrow on 'Merge' panel clearly showing no labelling on the tip). The pattern of distribution changes along the length of the tube, from clear location on the PM (transect a–a'), to mostly cytoplasmic towards the subapical area (c–c') and a transition zone (b–b'), where labelling is still observable on the PM. Insert corresponds to a forming callose plug (boxed area) and confirms the nature of the labelling in the PM on the tip-distal areas by two criteria: the labelling (1) contours perfectly the plug constriction, showing that it is absent from the cell wall, and (2) is clearly visible in the nascent stretches of membrane (white arrows) that will seal the two parts of the tube. (d) FM4-64 dye in red confirmed the PM localisation (transect d–d') of *At*CCC-GFP and its exclusion from the tip-proximal areas of the tube. Yet, at larger magnification and more sensitivity conditions, it is also obvious the accumulation of fluorescence on the cytoplasm, namely in particulate structures, specially in the tip-proximal areas (e) Pixel intensity profiles of transects a–a', b–b', c–c' (from c) and d–d' (from d). Despite substantial signal from the cytoplasm, PM peaks (asterisks) are still clearly observable even on widefield/non-confocal images of the tip-distal zones of short PTs. (f) Transgenic PTs overexpressing *At*SLAH3-YFP. Clear PM localisation of *At*SLAH3 is seen, specially at the shank. (images in (c) acquired on a Zeiss LSM 510 META using a ×40 1.4NA oil; images in (d) and (f) acquired on an Applied Precision Deltavision CORE system using the ×100 Uplan SAPO 1.4NA oil immersion objective and the ×60 1.2NA water immersion objective).

N-terminally tagged chimeras. Of relevance, all proteins visualised showed some cytoplasmic localisation, which suggests that they may mediate transport on other organelles. This result provided a plausible explanation for the increase in fluxes at the PM of double mutants, as absence of ion equilibrium from intracellular stores may lead to PM flux compensation.

Discussion

By employing the WC configuration of the patch-clamp technique in *A. thaliana* pollen protoplasts, with anion-based bath and pipette solutions, it was possible to identify and analyse distinct anionic current properties based on the loss of current by rundown, regulation by $[Ca^{2+}]_{cyt}$ and NPPB inhibition. To facilitate data analysis and better define their molecular properties, we analysed the $I_{initial}$ and I_{final} that are considered to correspond to individual anionic current populations, despite their obvious interdependence, and $I_{rundown}$, I_{NPPB} and $I_{inhibited}$ as their subpopulations. $I_{rundown}$, I_{NPPB} and $I_{inhibited}$ showed regulation by $[Ca^{2+}]_{cyt}$ and shared a strong outward rectification suggesting that the putative channels favoured the influx of anions. But, as the negative currents underwent rundown and a portion was also inhibited by NPPB, it is possible to conclude that the anionic transporters responsible for the currents described here displayed an ability to conduct both influx and efflux of anions, according to the anionic electrochemical gradient existent under physiological conditions. This conclusion is especially important, because, as previously analysed and discussed (Tavares *et al.*, 2011a), the current properties we describe could also account for the high magnitude effluxes of anions found at the tip of growing PTs when measured by vibrating probes.

In *A. thaliana*, the currents observed were regulated by $[Cl^-]_{out}$, presenting a decrease in the negative current properties when $[Cl^-]_{out}$ was lowered (Fig. 1j–m; Table S4). This behaviour was not observed in lily pollen anionic currents (Tavares *et al.*, 2011a). Furthermore, *At* channels were two times more permeable to NO_3^- than to Cl^- (Fig. 1l,m; Table S5), while in lily the channels were only slightly more permeable to NO_3^- than to Cl^- ($P_{NO_3}/P_{Cl} \approx 1.2$). S-type anion channels found in guard cells of different species, although with very similar characteristics, differ in their sensitivity to known anion channel blockers (Linder & Raschke, 1992; Dieudonne *et al.*, 1997; Grabov *et al.*, 1997; Forestier *et al.*, 1998; Frachisse *et al.*, 1999) as do the TMEM16A Ca^{2+}-activated Cl^- channel from *Xenopus laevis* oocytes and mouse (Schroeder *et al.*, 2008; Yang *et al.*, 2008). Furthermore, we showed that *At*TMEM16 seems to specifically discriminate NO_3^-, sharing this property with NPF2.4 (Li *et al.*, 2016) as the two only examples of chloride-specific transporters in plants so far described.

Electrophysiological characterisation of mutant protoplasts revealed a redundancy and coordination between different channels

The currents measured from PT protoplasts of three of the four mutants presented significant differences to those measured for the WT group, namely: (1) a higher elicited $I_{initial}$ in *slah3*$^{-/-}$ and *tmem16*$^{-/-}$ protoplasts; and (2) reduced I_{final} in *almt12*$^{-/-}$ for the negative V_m. In addition, the three mutants depicted: (3) increased %Rundown specifically for the negative V_m; and (4) different responses to NPPB. The currents elicited from the double mutant line *almt12*$^{-/-}$;*slah3*$^{-/-}$ presented for the negative V_m: (1) a significant decrease in $I_{initial}$, I_{final} and increased %Rundown when compared with the WT and to each single mutant; and (2) a higher %Inhibition in relation to *slah3*$^{-/-}$. These results are suggestive of the existence of other levels of regulation of anion transport across the PM, and different types of compensation. In *A. thaliana* leaves, SLAH3 was recently shown to function as an essential negative regulator of inward K^+-channels and stomatal opening (Zhang *et al.*, 2016). In mammalian cells, one of the best-recognised functions of the Cl^- channel CFTR is the ability to modulate the functioning of other transporters (Greger & Windhorst, 1996). For example, in salt-absorbing sweat ducts, activation of CFTR triggers the stimulation of epithelial Na^+ channels (Schwiebert *et al.*, 1999). Conversely, differential trafficking to different subcellular organelles was recently found to trigger compensation by increase of PM Ca^{2+} fluxes in some GLR channels (Wudick *et al.*, 2018).

Pinpointing the candidate anionic transporters in growing PTs

The uneven distribution of anion fluxes is reflected by the intracellular gradient of cytosolic Cl^- with a high $[Cl^-]$ domain *c.* 20–40 μm behind the tip, especially visible upon extracellular Cl^- elevation, and lower at the tip (Gutermuth *et al.*, 2013, 2018). The minimal model of a mechanism behind it would be an uneven allocation of anion channels, such that an active outward-directed anion translocation process should exist in the tip and inward activity in the shank (Zonia *et al.*, 2002). GFP tagging showed that *At*SLAH3 localises to the shank, but is also visible at the tip. The cotransporters *At*CCC and *At*TMEM16, are preferentially localised at the shank and grain. Gutermuth *et al.* (2013) showed through biolistic transformation of *N. tabacum* pollen with *At*SLAH3−YFP a similar uniform PM localisation along the shank. Conversely, a study of *At*CCC in *A. thaliana* and grapevine could localise this cotransporter to the Golgi and *trans*-Golgi network (Henderson *et al.*, 2015). Nevertheless, localisation on the PM using immunolabelling was described for rice CCC (Chen *et al.*, 2016).

The most parsimonious interpretation of our electrophysiological and localisation data would therefore be to assign *At*SLAH3 and *At*ALMT12 as the channels responsible for the large oscillatory effluxes at the tip and, together with *At*CCC and *At*TMEM16, for the non-oscillatory influx measured in the shank. Polarity would be therefore achieved by a combination of differential sorting of channels and differential regulation of *At*SLAH3 features between the tip and the shank. This hypothesis is compatible with more recent accounts of interplay between *At*SLAH3 and CPKs (Gutermuth *et al.*, 2018). A possible model incorporating these interpretations is offered in Fig. 5. Of relevance, ALMT channels have also recently been shown to facilitate the transport of GABA, therefore facilitating an equilibrium between inside and outside and assuring activation of currents (Ramesh *et al.*, 2018).

*At*TMEM16 is an H^+/anion cotransporter

We provide the first identification of *At*TMEM16 as a putative H^+/anion cotransporter in the PM of *A. thaliana* pollen protoplasts with an electrophysiological and functional phenotype. Several reports have demonstrated previously that putative anionic channels in plants are H^+/Cl^- transporters (Accardi & Miller, 2004; Scheel *et al.*, 2005; Pusch *et al.*, 2006). Given the importance of H^+ as a second messenger (Prolo & Goodman, 2008), we hypothesised that pH or H^+ can regulate the observed anionic currents in the PM of PGs, resulting in the observed differences. Internal pH was demonstrated to have an equally important role in regulating the anionic currents. The conditions tested mimic the two major intracellular domains in the PT in terms of pH, an acidic tip and an alkaline shank. Our results evidenced a large increase in anionic current under more acidic internal pH conditions ($pH_{in} = 6.8$), in line with that observed in growing PTs, which showed massive anionic effluxes at the acidic tip (Zonia *et al.*, 2002).

While the response to $[Cl^-]$ changes is similar between WT and the *tmem16*$^{-/-}$ mutant, the same is not true for $[NO_3^-]$ changes. In the *tmem16*$^{-/-}$ mutant, currents under high $[NO_3^-]_{out}$ are reduced up to a third of their equivalent amplitudes under high $[Cl^-]_{out}$ in the mutant. These results suggest that both ions are still being transported across the membrane

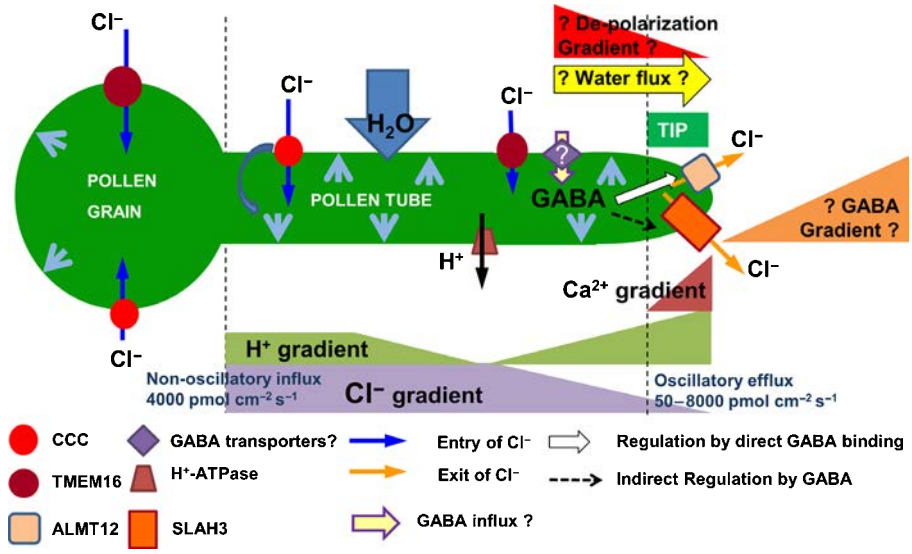

Fig. 5 Model depicting a putative feedback-regulation of pollen tube (PT) growth by γ-aminobutyric acid (GABA), pH and Ca^{2+} through anionic transporters during sexual reproduction in flowering plants. Blue and orange arrows indicate anion influx at the grain and shank and efflux at the tip; Cl^-, Ca^{2+} and H^+ gradients are shown. Upon germination PTs are exposed to increasing GABA concentrations along the pistil (20 μM in the stigma, 60 μM in the style, 110 μM in ovary walls, 160 μM in the septum and 500 μM in the integuments, Palanivelu *et al.*, 2003). GABA enters the PT through GABA transporters, a function recently attributed to aluminum-activated malate transporter (ALMT) channels (Ramesh *et al.*, 2018), directly binding to ALMT12. This regulation causes ionic unbalance followed by the passive flow of water according to the osmotic gradient, which in turn supports and signals for growth. pH and Ca^{2+} further regulate other anionic channels such as AtTMEM16 and AtSLAH3 (Gutermuth *et al.*, 2018).

and both contribute to the equilibrium potential, but the channels still present in the PM of the mutant show higher permeability to Cl^- than NO_3^-.

Regulation of anionic currents by GABA in protoplasts from fully hydrated pollen grains

A shared region between the mammalian $GABA_A$ receptor and ALMT members, was previously found using MEME analysis (Motif-based sequence analysis tools; Fig. S5; Ramesh *et al.*, 2015). The previous results were mostly obtained by heterologous expression of the channel, but here we show that GABA reduces the overall current measured in protoplasts from fully hydrated PGs, and provide two strong arguments that this regulation is carried out by a direct interplay between *At*ALMT12 and GABA, namely: (1) PTs from two independent alleles of *almt12*$^{-/-}$ were insensitive to muscimol, while in WT this drug significantly inhibited PT growth; and (2) heterologous expression of the *At*ALMT12 protein in the mammalian cell line COS-7 produced voltage-dependent effluxes (inward currents) sensitive to GABA. Our results provided the first genetic evidence that *At*ALMT12 is a GABA receptor. The previously observed growth modulation of GABA on *A. thaliana* PTs by our group and others (Palanivelu *et al.*, 2003; Ramesh *et al.*, 2015) could be due to this interaction.

Acknowledgements

Supported by National Science Foundation (MCB1616437/2016, MCB1714993/2017) and Fundação para a Ciência e Tecnologia- FCT (PTDC/QUI/64359/2006, BIA-BCM/108044/2008, PTDC/BEX-BCM/0376/2012, PTDC/BIA-PLA/4018/2012; fellowships SFRH/BD/27399/2006, SFRH/BD/63694/2009, SFRH/BD/69168/2010). MG was supported by ARC (CE140100008 and FT130100709). We thank R. Hedrich (Univ. Würzburg) and J. M. Colmenero-Flores and M. Talón (IVIA, Valencia) for Arabidopsis lines.

Author contributions

PD, PND and BT designed and performed most experiments, analysed the data, and wrote the manuscript; MTP, KRK and MMW performed experiments; AB supervised the experiments and conceived the project; MG designed GABA experiments; JAF conceived and supervised the overall project, designed experiments, analysed data and wrote the manuscript. All authors revised the manuscript PD and PND contributed equally to this work.

ORCID

Pedro N. Dias https://orcid.org/0000-0001-6719-4637
Patrícia Domingos https://orcid.org/0000-0001-7011-9240
José A. Feijó https://orcid.org/0000-0002-1100-5478
Matthew Gilliham https://orcid.org/0000-0003-0666-3078
Kai R. Konrad https://orcid.org/0000-0003-4626-5429
Maria Teresa Portes https://orcid.org/0000-0001-5668-0605
Bárbara Tavares https://orcid.org/0000-0002-4048-8915
Michael M. Wudick https://orcid.org/0000-0002-4332-369X

References

Accardi A, Miller C. 2004. Secondary active transport mediated by a prokaryotic homologue of ClC Cl^- channels. *Nature* **427**: 803–807.

Becq F. 1996. Ionic channel rundown in excised membrane patches. *Biochemica et Biophysica Acta* **1286**: 53–63.

Binder KA, Wegner LH, Heidecker M, Zimmermann U. 2003. Gating of Cl-currents in protoplasts from the marine alga *Valonia utricularis* depends on the transmembrane Cl- gradient and is affected by enzymatic cell wall degradation. *Journal Membrane Biology* **191**: 165–178.

Boavida LC, Borges F, Becker JD, Feijó JA. 2011. Whole genome analysis of gene expression reveals coordinated activation of signaling and metabolic pathways during pollen–pistil interactions in Arabidopsis. *Plant Physiology* **155**: 2066–2080.

Boavida LC, Vieira AM, Becker JD, Feijó JA. 2005. Gametophyte interaction and sexual reproduction: how plants make a zygote. *The International Journal of Developmental Biology* **49**: 615–632.

Caputo A, Caci E, Ferrera L, Pedemonte N, Barsanti C, Sondo E, Pfeffer U, Ravazzolo R, Zegarra-Moran O, Galietta LJV. 2008. TMEM16A, a membrane protein associated with calcium-dependent chloride channel activity. *Science* **322**: 590–594.

Cenis JL. 1992. Rapid extraction of fungal DNA for PCR amplification. *Nucleic Acids Research* **20**: 2380.

Certal AC, Almeida RB, Carvalho LM, Wong E, Moreno N, Michard E, Carneiro J, Rodriguéz-Léon J, Wu H-M, Cheung AY *et al.* 2008. Exclusion of a proton ATPase from the apical membrane is associated with cell polarity and tip growth in *Nicotiana tabacum* pollen tubes. *Plant Cell* **20**: 614–634.

Chen ZC, Yamaji N, Fuji-Kashino M, Ma JF. 2016. A cation-chloride co-transporter gene is required for cell elongation and osmoregulation in CCC rice. *Plant Physiology* **171**: 494–507.

Clough SJ, Bent AF. 1998. Floral dip: a simplified method for Agrobacterium-mediated transformation of *Arabidopsis thaliana*. *The Plant Journal* **16**: 735–743.

Colmenero-Flores JM, Martínez G, Gamba G, Vázquez N, Iglesias DJ, Brumós J, Talón M. 2007. Identification and functional characterization of cation-chloride cotransporters in plants. *The Plant Journal* **50**: 278–292.

Courjaret R, Hodeify R, Hubrack S, Ibrahim A, Dib M, Daas S, Machaca K. 2016. The Ca^{2+}-activated Cl channel Ano1 controls microvilli length and membrane surface area in the oocyte. *Journal of Cell Science* **129**: 2548–2558.

Dieudonné S, Forero ME, Llano I. 1997. Two different conductances contribute to the anion currents in *Coffea arabica* protoplasts. *Journal of Membrane Biology* **159**: 83–94.

Edwards K, Johnstone C, Thompson C. 1991. A simple and rapid method for the preparation of plant genomic DNA for PCR analysis. *Nucleic Acids Research* **19**: 1349.

Fan L-M, Wang Y-F, Wang H, Wu W-H. 2001. *In vitro* Arabidopsis pollen germination and characterization of the inward potassium currents in Arabidopsis pollen grain protoplasts. *Journal of Experimental Botany* **52**: 1603–1614.

Feijó JA. 2010. The mathematics of sexual attraction. *Journal of Biology* **9**: 18.

Forestier C, Bouteau F, Leonhardt N, Vavasseur A. 1998. Pharmacological properties of slow anion currents in intact guard cells of *Arabidopsis*. Application of the discontinuous single-electrode voltage–clamp to different species. *Pflügers Archiv European Journal of Physiology* **436**: 920–927.

Frachisse J-M, Thomine S, Colcombet J, Guern J, Barbier-Brygoo H. 1999. Sulfate is both a substrate and an activator of the voltage-dependent anion channel of Arabidopsis hypocotyl cells. *Plant Physiology* **121**: 253–262.

Geiger D, Maierhofer T, Al-Rasheid KAS, Scherzer S, Mumm P, Liese A, Ache P, Wellmann C, Marten I, Grill E *et al.* 2011. Stomatal closure by fast abscisic acid signaling is mediated by the guard cell anion channel SLAH3 and the receptor RCAR1. *Science Signaling* **4**: ra32.

Gögelein H. 1988. Chloride channels in epithelia. *Biochimica et Biophysica Acta* **947**: 521–547.

Grabov A, Leung J, Giraudat J, Blatt MR. 1997. Alteration of anion channel kinetics in wild-type and abi1-1 transgenic *Nicotiana benthamiana* guard cells by abscisic acid. *Plant Journal* **12**: 203–213.

Greger R, Windhorst U, eds. 1996. *Comprehensive human physiology: from cellular mechanisms to integration.* Heidelberg, Berlin, Germany: Springer.

Gutermuth T, Herbell S, Lassig R, Brosché M, Romeis T, Feijó JA, Hedrich R, Konrad KR. 2018. Tip-localized Ca^{2+} permeable channels control pollen tube growth via kinase-dependent R- and S-type anion channel regulation. *New Phytologist* **218**: 1089–1105.

Gutermuth T, Lassig R, Portes M-T, Maierhofer T, Romeis T, Borst J-W, Hedrich R, Feijó JA, Konrad KR. 2013. Pollen tube growth regulation by free anions depends on the interaction between the anion channel SLAH3 and calcium-dependent protein kinases CPK2 and CPK20. *Plant Cell* **25**: 4525–4543.

Hamilton ES, Jensen GS, Maksaev G, Katims A, Sherp AM, Haswell ES. 2015. Mechanosensitive channel MSL8 regulates osmotic forces during pollen hydration and germination. *Science* **350**: 438–441.

Henderson SW, Wege S, Qiu J, Blackmore DH, Walker AR, Tyerman S, Walker RR, Gilliham M. 2015. Grapevine and Arabidopsis cation-chloride cotransporters localise to the Golgi and trans-Golgi network and indirectly influence long-distance ion homeostasis and plant salt tolerance. *Plant Physiology* **169**: 2215–2229.

Krogsgaard-Larsen P, Johnston GA. 1978. Structure-activity studies on the inhibition of GABA binding to rat brain membranes by muscimol and related compounds. *Journal of Neurochemistry* **30**: 1377–1382.

Li B, Byrt C, Qiu J, Baumann U, Hrmova M, Evrard A, Johnson AAT, Birnbaum KD, Mayo GM, Jha D *et al.* 2016. Identification of a stellar-localised transport protein that facilitates root-to-shoot transfer of chloride in Arabidopsis. *Plant Physiology* **170**: 1014–1029.

Linder B, Raschke K. 1992. A slow anion channel in guard cells, activating at large hyperpolarization, may be principal for stomatal closing. *The Federation of European Biochemical Societies Letters* **313**: 27–30.

Marty A, Neher E. 1995. Tight-seal whole-cell recording. In: Sakmann B, Neher E, eds. *Single channel recording.* New York, NY, USA: Plenum, 31–52.

Meyer S, Mumm P, Imes D, Endler A, Weder B, Al-Rasheid KAS, Geiger D, Marten I, Martinoia E, Hedrich R. 2010. AtALMT12 represents an R-type anion channel required for stomatal movement in Arabidopsis guard cells. *The Plant Journal* **63**: 1054–1062.

Mouline K, Véry A, Gaymard F, Boucherez J, Pilot G, Devic M, Bouchez D, Thibaud J, Sentenac H. 2002. Pollen tube development and competitive ability are impaired by disruption of a Shaker K(+) channel in Arabidopsis. *Genes & Development* **16**: 339–350.

Nicholson SH, Suckling CJ, Iversen LL. 1979. GABA analogues: conformational analysis of effects on [^{3}H]GABA binding to postsynaptic receptors in human cerebellum. *Journal of Neurochemistry* **32**: 249–252.

Palanivelu R, Brass L, Edlund AF, Preuss D. 2003. Pollen tube growth and guidance is regulated by POP2, an Arabidopsis gene that controls GABA levels. *Cell* **114**: 47–59.

Paulino C, Kalienkova V, Lam AKM, Neldner Y, Dutzler R. 2017. Activation mechanism of the calcium-activated chloride channel TMEM16A revealed by cryo-EM. *Nature* **552**: 421–425.

Pedemonte N, Galietta LJV. 2014. Structure and function of TMEM16 proteins (Anoctamins). *Physiological Reviews* **94**: 419–459.

Pina C, Pinto F, Feijó JA, Becker JD. 2005. Gene family analysis of the Arabidopsis pollen transcriptome reveals biological implications for cell growth, division control, and gene expression regulation. *Plant Physiology* **138**: 744–756.

Prado AM, Colaço R, Moreno N, Silva AC, Feijó JA. 2008. Targeting of pollen tubes to ovules is dependent on nitric oxide (NO) signaling. *Molecular Plant* **1**: 703–14.

Prolo LM, Goodman MB. 2008. Physiology: keeping it regular with protons. *Nature* **452**: 35–36.

Pusch M, Zifarelli G, Murgia AR, Picollo A, Babini E. 2006. Channel or transporter? The CLC saga continues. *Experimental Physiology* **91**: 149–152.

Ramesh SA, Kamran M, Sullivan W, Chirkova L, Okamoto M, Degryse F, McLaughlin M, Gilliham M, Tyerman SD. 2018. Aluminum-activated malate transporters can facilitate GABA transport. *Plant Cell* **30**: 1147–1164.

Ramesh SA, Tyerman SD, Xu B, Bose J, Kaur S, Conn V, Domingos P, Ullah S, Wege S, Shabala S *et al.* 2015. GABA signalling modulates plant growth by directly regulating the activity of plant-specific anion transporters. *Nature Communications* **6**: 7879.

Scheel O, Zdebik AA, Lourdel S, Jentsch TJ. 2005. Voltage-dependent electrogenic chloride/proton exchange by endosomal CLC proteins. *Nature* **436**: 424–427.

Schroeder BC, Cheng T, Jan YN, Jan LY. 2008. Expression cloning of TMEM16A as a calcium-activated chloride channel subunit. *Cell* **134**: 1019–1029.

Schwiebert LM, Estell K, Propst SM. 1999. Chemokine expression in CF epithelia: implications for the role of CFTR in RANTES expression. *American Journal of Physiology* **276**: C700–C710.

Tanaka I, Kitazume C, Ito M. 1987. The isolation and culture of lily pollen protoplasts. *Plant Science* **50**: 205–211.

Tavares B, Dias PN, Domingos P, Moura TF, Feijó JA, Bicho A. 2011a. Calcium-regulated anion channels in the plasma membrane of *Lilium longiflorum* pollen protoplasts. *New Phytologist* **192**: 45–60.

Tavares B, Domingos P, Dias PN, Feijó JA, Bicho A. 2011b. The essential role of anionic transport in plant cells: the pollen tube as a case study. *Journal of Experimental Botany* **62**: 2273–2298.

Yang YD, Cho H, Koo JY, Tak MH, Cho Y, Shim W-S, Park SP, Lee J, Lee B, Kim B-M *et al.* 2008. TMEM16A confers receptor-activated calcium-dependent chloride conductance. *Nature* **455**: 1210–1215.

Wudick MM, Michard E, Oliveira C, Feijó JÁ. 2018. Comparing plant and animal glutamate receptors: common traits but different fates? *Journal of Experimental Botany* **69**: 4151–4163.

Zhang A, Ren H-M, Tan Y-Q, Qi G-N, Yao F-Y, Wu G-L, Yang L-W, Hussain J, Sun S-J, Wang Y-F. 2016. S-type anion channels SLAC1 and SLAH3 function as essential negative regulators of inward K^+ channels and stomatal opening in Arabidopsis. *Plant Cell* **28**: 949–965.

Zonia L, Cordeiro S, Tupý J, Feijó JA. 2002. Oscillatory chloride efflux at the pollen tube apex has a role in growth and cell volume regulation and is targeted by inositol 3,4,5,6-tetrakisphosphate. *Plant Cell* **14**: 2233–2249.

Supporting Information

Additional Supporting Information may be found online in the Supporting Information section at the end of the article.

Fig. S1 Variation of the average current density and its properties with the tested $[Ca^{2+}]_{cyt}$.

Fig. S2 Typical activation and tail currents from *Arabidopsis thaliana* wild-type and two different *tmem16*$^{-/-}$ alleles under different pH_{out} conditions.

Fig. S3 Competition assays for the *tmem16*$^{-/-}$ mutant.

Fig. S4 *Arabidopsis thaliana* steady-state anionic currents acquired from wild-type and *almt12*$^{-/-}$ mutant plants 10 min after entering whole-cell (WC) (I_{inital}) in the absence or presence of $[10\ \mu M]_{in}$ muscimol.

Fig. S5 Variation in the residues of the identified GABA-binding motif between ALMT proteins.

Fig. S6 Growth rate collected from *Arabidopsis thaliana* wild-type and from the second independent mutant line ccc-2 pollen tubes.

Fig. S7 Widefield fluorescence microscopy images of transgenic pollen tubes overexpressing GFP-fused *At*ALMT12 protein.

Methods S1 Plants, culture conditions and pollen grain collection.

Methods S2 Identification of *A. thaliana* mutant lines and their morphology.

Methods S3 Cell line culture and transient transfection.

Methods S4 Live-cell and confocal imaging.

Methods S5 Protoplast isolation.

Methods S6 Electrophysiology.

Methods S7 Pollen germination and anion-selective self-referencing probe analysis of Cl^- fluxes.

Methods S8 Data analysis.

Table S1 Primers used to genotype each mutant line and to generate transgenic lines.

Table S2 Composition of the recording solutions.

Table S3 Equilibrium potentials for the permeable ions in the recording solutions.

Table S4 Anion current parameters calculated with different $[Ca^{2+}]_{cyt}$.

Table S5 Anion current parameters calculated before and after BSE1 (B1/P1 to B2), BSE2 (B1/P1 → B3) and BSE3 (B4/P4 → B5).

Video S1 Time-lapse Z-stack sequence images (Widefield) of a pollen tube overexpressing *At*SLAH3–GFP.

Video S2 Time-lapse Z-stack sequence images of an overexpressing *AtTMEM16*–GFP pollen tube.

Please note: Wiley Blackwell are not responsible for the content or functionality of any Supporting Information supplied by the authors. Any queries (other than missing material) should be directed to the *New Phytologist* Central Office.